

## Prestellar Cores in Turbulent Clouds II. Properties of Critical Cores

SANGHYUK MOON<sup>1</sup> AND EVE C. OSTRIKER<sup>1</sup>

<sup>1</sup>*Department of Astrophysical Sciences, Princeton University, Princeton, NJ 08544, USA*

### ABSTRACT

A fraction of the dense cores within a turbulent molecular cloud will eventually collapse, leading to star formation. Identifying the physical criteria for cores to become unstable, and analyzing critical core properties, thus constitutes a necessary step toward the complete theory of star formation. Here we quantify the characteristics of an ensemble of “critical cores” on the verge of collapse. This critical epoch was identified in a companion paper, which followed the dynamical evolution of prestellar cores in numerical simulations of turbulent, self-gravitating clouds. We find that radial profiles of density and turbulent velocity dispersion in individual critical cores are consistent with our new model for turbulent equilibrium spheres (TESSs). While a global linewidth–size relation exists for a cloud with given size and Mach number, the turbulent scaling relations around each core exhibit significant variations, locally regulating the critical density for a core to become unstable. As a result, there is no single density threshold for collapse; instead, cores collapse at a range of densities determined by the local sonic scale and gravitational potential environment, with a distribution expected for TESSs with a limited range of turbulent velocity dispersion. The critical cores in our simulations are mostly transonic; we do not find either purely thermal or highly turbulent cores. We find that the core mass function (CMF) of critical cores peaks around the characteristic mass scale associated with the large-scale cloud properties. We highlight the importance of constructing the CMF at the critical time instead of sink particle mass functions, and derive the resolution requirements to unambiguously identify the peak of the CMF.

### 1. INTRODUCTION

Dense cores are transient structures within turbulent giant molecular clouds (GMCs), with their properties continuously changing in space and time (see Bergin & Tafalla 2007; di Francesco et al. 2007; McKee & Ostriker 2007; André et al. 2014; Offner et al. 2014; Padoan et al. 2014, for related reviews). While the physical properties of *prestellar* cores — which ultimately collapse, leading to star formation — are of great interest, it has not been clear exactly what the criterion is for a given core to become unstable and therefore unambiguously “prestellar.” In observational surveys, the simplest working definition for prestellar candidates is cores that appear gravitationally bound, based on estimates of their internal energy, although more detailed criteria have also been applied (e.g. André et al. 2000; Könyves et al. 2015). However, simulations that trace the evolution of dense structures show that many stochastically cycle through different phases (due to their turbulent environment), rather than following a single evolution-

ary sequence, and in particular cores with “prestellar” characteristics sometimes subsequently disperse (Offner et al. 2022).

Notwithstanding the ambiguities in recognizing prestellar cores, their very nature — objects that will collapse to form a star or stellar system in the near future — provides at least two physically meaningful common reference points in time shared across all cores: (1) The time when they *initiate* gravitational runaway (hereafter “critical time”) and (2) the instant they *complete* it by forming a nascent protostar at the center (“collapse time”). While these milestones would be essentially impossible to pinpoint in observations, they can be identified on an individual core basis within numerical simulations of gravo-turbulent fragmentation.

The second of the two above events is easier to pick out in simulations, since this is when runaway collapse leads to a  $\rho \propto r^{-2}$  singular density profile (Larson 1969; Penston 1969).<sup>1</sup> In particular, in numerical simulations where collapsing centers are replaced with sink parti-

<sup>1</sup> Strictly speaking, it is only at the center of this power-law profile that a protostar-disk system begins to grow.

cles, the collapse time of each core can be identified as the moment when a sink particle is created. For example, Gong & Ostriker (2015), Padoan et al. (2020), and Pelkonen et al. (2021) used the closest snapshot to the creation time of each sink particle to define their “progenitor core” as a gravitationally bound region around the site where the sink is created.

By measuring the core mass at each core’s collapse time, Gong & Ostriker (2015) demonstrated that the core mass function (CMF) has a well-defined peak which converges with increasing numerical resolution. Pelkonen et al. (2021), taking a slightly different approach, varied the resolution for the clumpfind algorithm rather than the underlying simulation resolution, and also found convergence in the CMF at the time of collapse. In the majority of numerical studies of gravo-turbulent fragmentation, however, it is not the CMF at a characteristic epoch for each core or sink’s evolution that is measured, but instead the sink particle mass function (SMF) at an arbitrarily selected time common to all particles (e.g., Haugbølle et al. 2018; Lee & Hennebelle 2018; Guszejnov et al. 2020). The resulting SMF has not shown numerically converging behavior, unlike the CMF based on individual collapse times (see, however, Haugbølle et al. 2018; Pelkonen et al. 2021). As we shall discuss, the reason for the difference between CMF convergence and SMF non-convergence likely relates to fragmentation in late stages of evolution. But in any case, in order to test theories of turbulent fragmentation that are the basis for models of the initial mass function (e.g., Padoan & Nordlund 2002; Hennebelle & Chabrier 2008; Hopkins 2012), it is necessary to construct the CMF itself at characteristic epochs of evolution.

While the collapse time provides a convenient reference point and can be easily identified in numerical simulations, it is the *critical time* that is most relevant for the point of comparison to theories. Collins et al. (2024), by analyzing the collapse histories of simulated cores via tracer particles, found that there exists a characteristic epoch after which mass is rapidly delivered to the core center, raising the core density in a runaway fashion. Based on this observation they defined a proxy for the critical time (termed “singularity time” in their work) by choosing a threshold on the density time derivative. They found that, as each core approaches its critical time, the radial density profiles of cores develop a characteristic core–envelope structure while the mean radial and tangential velocities exhibit a common behavior of increasing in magnitude with increasing radius. The identification of this characteristic epoch reveals a common physical process occurring in an ensemble of cores that is otherwise blurred by evolution. However, the

question of what determines this critical time still remains to be answered.

Related to the critical time is a common narrative for the evolution of prestellar cores, where certain critical conditions trigger gravitational runaway (McKee & Ostriker 2007; André et al. 2014; Offner et al. 2014; Padoan et al. 2014). Among others, the Bonnor-Ebert (BE) sphere and its stability property (Ebert 1955; Bonnor 1956; Ebert 1957) have often been used as a theoretical tool for determining critical conditions (e.g., Krumholz & McKee 2005; Padoan & Nordlund 2011). However, the applicability of the BE model to cores within turbulent molecular clouds is limited, because (1) real cores exist as a part of a turbulent continuum unlike an isolated BE sphere truncated by “external pressure,” and (2) the model does not account for internal turbulent velocities expected for cores forming within a turbulent cloud.

In a series of papers, we have begun a comprehensive analysis of prestellar core evolution to address the limitations pertaining to the BE model and to answer the question of exactly what triggers the onset of collapse. In Moon & Ostriker (2024a, hereafter Paper I), we developed a new theoretical model for equilibrium spherically-symmetric cores supported by both thermal and turbulent pressure, with the solutions obtained by directly solving the time-steady, angle-averaged equations of hydrodynamics. A distinguishing feature of the resulting family of solutions, which we term the turbulent equilibrium sphere (TES), is that the turbulent pressure naturally arises from a power-law velocity structure function rather than from a phenomenological equation of state. The TES model also enjoys a useful behavior of reducing to the BE model in the limit of vanishing turbulent velocities. Paper I found that, similar to the case for BE spheres, solutions can be classified as stable or unstable to radial perturbations. For a given set of turbulence parameters and central density, cores exceeding a certain critical size are unstable. The radius, mass, and center-to-edge density contrast of critical TESs all increase with increasing turbulent velocity dispersion (or equivalently, decreasing sonic scale). This implies that a nascent core forming in a highly turbulent region would initially be in the stable, subcritical regime.

Based on the stability properties of TESs and from a general consideration of tidal gravitational fields in core-forming regions, Paper I proposed an evolutionary scenario for “successful” prestellar cores formed by converging turbulent flows. In this scenario, nascent cores evolve in the direction of increasing density (as mass is added) and decreasing turbulence (as dissipation pro-

gresses). When converging flows are strong enough or turbulence sufficiently dissipates, the critical radius  $r_{\text{crit}}$  moves inside the “tidal radius”  $r_{\text{tidal}}$  set by the landscape of the gravitational potential, and a core becomes unstable and collapses. Otherwise, it remains stable and is eventually dispersed by turbulence (see Figure 11 of Paper I for a schematic illustration for this scenario). To test this scenario and identify the critical conditions for collapse, in Moon & Ostriker (2024b) (hereafter Paper II) we conducted and carefully analyzed a suite of numerical simulations of turbulent, self-gravitating clouds. Paper II presents results from a comprehensive analysis of each core’s dynamical evolution from its formation, through the onset of collapse, to the point when the central density blows up, signaling the beginning of the protostellar phase. By measuring radial forces acting within the cores over time, Paper II directly identified the critical time when the net radial force becomes negative, instigating runaway collapse. We found good agreement between the empirically identified critical time and the epoch when a core is predicted to be unstable according to the TES model, thus providing an answer as to what determines the critical time.

In this paper, we analyze the simulation results of Paper II at the critical time of each core to investigate the physical properties of prestellar cores at the onset of collapse. We shall show that the cores defined at their respective critical time (referred to as “critical cores” throughout this work) are mostly transonic in terms of their internal turbulence (turbulent Mach number  $\sim 0.5$ –1.5), with their structure overall consistent with the TES model. We shall also show that the local turbulent scaling relations within each core exhibit significant variations above and below the average linewidth–size relation for the entire cloud, with higher density in more turbulent critical cores. As a result, there is a wide range of critical densities for collapse, rather than a single threshold density. We shall also present statistical distributions of core masses, sizes, densities, durations of different evolutionary stages, and accretion rates.

The remainder of this paper is organized as follows. In Section 2, we define key physical quantities related to our TES model and numerical simulations. In Section 3, we first (Section 3.1) present the radial density and velocity dispersion profiles of critical cores and compare them with the TES models. We then (Section 3.2) show that the locally constructed linewidth–size relations exhibit significant variations around the mean relation, causing cores to become unstable at a wide range of densities (Section 3.3). We also present probability distributions of various physical quantities measured for critical cores, including the CMF (Sec-

tion 3.4). Section 4 presents the evolution of the mass inflow rates and, by using them, characterizes evolutionary timescales at each stage. We discuss implications of our results in Section 5 and conclude in Section 6.

## 2. KEY DEFINITIONS

In this section, we provide key concepts and definitions of physical quantities that will be used throughout the paper. We refer the reader to Paper I and Paper II for complete descriptions of our TES model and numerical simulations, respectively.

The radius and mass scales most relevant to isothermal self-gravitating objects supported entirely by thermal pressure are the critical BE radius and mass given by

$$R_{\text{BE}}(\bar{\rho}) = 0.762 \frac{c_s}{G^{1/2} \bar{\rho}^{1/2}}, \quad (1)$$

$$M_{\text{BE}}(\bar{\rho}) \equiv \frac{4\pi}{3} \bar{\rho} R_{\text{BE}}^3(\bar{\rho}) = 1.86 \frac{c_s^3}{G^{3/2} \bar{\rho}^{1/2}}, \quad (2)$$

where  $c_s = (kT/\mu)^{1/2}$  is the isothermal sound speed with temperature  $T$  and mean molecular weight  $\mu$ ,  $G$  is the gravitational constant, and  $\bar{\rho}$  is the average density within a core.

Paper I generalized these results for TESs characterized by the power-law linewidth–size relation of the form

$$\langle \delta v_r^2 \rangle_\rho^{1/2} = c_s \left( \frac{r}{r_s} \right)^p = c_s \left( \frac{\xi}{\xi_s} \right)^p, \quad (3)$$

where  $\delta v_r \equiv v_r - \langle v_r \rangle_\rho$  is the radial velocity fluctuation,  $r_s$  is the sonic radius, and  $p$  is the power-law index. In the second equality,

$$\xi \equiv \frac{\sqrt{4\pi G \rho_c} r}{c_s} \quad (4)$$

is the dimensionless radius normalized with respect to the central density  $\rho_c$ , which also defines the dimensionless sonic radius  $\xi_s$  where  $r = r_s$ . The angled bracket in Equation (3) is a mass-weighted angle-averaging operator defined by

$$\langle Q \rangle_\rho \equiv \frac{\oint_{4\pi} \rho Q d\Omega}{\oint_{4\pi} \rho d\Omega}, \quad (5)$$

where  $\rho$  is gas density and  $Q$  is a physical quantity to be averaged. It is related to the volume-weighted average

$$\langle Q \rangle \equiv \frac{1}{4\pi} \oint_{4\pi} Q d\Omega \quad (6)$$

by  $\langle Q \rangle_\rho \equiv \langle \rho Q \rangle / \langle \rho \rangle$ .

Under a given turbulent velocity field defined by Equation (3), there exists a family of quasi-equilibrium TES

solutions parametrized by  $\xi_s$  and  $p$ . The critical radius and mass of these solutions are found to be

$$r_{\text{crit}}(\bar{\rho}) = \left(\frac{3}{4\pi}\right)^{1/2} \left(\frac{m_{\text{crit}}}{\xi_{\text{crit}}}\right)^{1/2} \frac{c_s}{G^{1/2}\bar{\rho}^{1/2}}, \quad (7)$$

$$M_{\text{crit}}(\bar{\rho}) = \left(\frac{3}{4\pi}\right)^{1/2} \left(\frac{m_{\text{crit}}}{\xi_{\text{crit}}}\right)^{3/2} \frac{c_s^3}{G^{3/2}\bar{\rho}^{1/2}}, \quad (8)$$

where we provide solutions for the dimensionless quantities  $m_{\text{crit}}$  and  $\xi_{\text{crit}}$  as functions of  $p$  and  $\xi_s$  (see Equations (56)–(57) of Paper I for alternative expressions of  $r_{\text{crit}}$  and  $M_{\text{crit}}$  based on the center and edge densities). At a given  $\bar{\rho}$ , both  $r_{\text{crit}}$  and  $M_{\text{crit}}$  decrease with increasing  $\xi_s$ , approaching  $R_{\text{BE}}$  and  $M_{\text{BE}}$  in the limit  $\xi_s \rightarrow \infty$  (see Figures 4 and 8 of Paper I).

For  $p = 0.5$ , Paper I found approximate relations to characterize how turbulence enhances the critical radius and mass for given mean density:

$$r_{\text{crit}}(\bar{\rho}) \approx R_{\text{BE}}(\bar{\rho}) \left(1 + 0.5 \frac{\sigma_{1\text{D}}^2}{c_s^2}\right)^{1/3}, \quad (9)$$

$$M_{\text{crit}}(\bar{\rho}) \approx M_{\text{BE}}(\bar{\rho}) \left(1 + 0.5 \frac{\sigma_{1\text{D}}^2}{c_s^2}\right), \quad (10)$$

which are valid within relative error of 5% for  $\sigma_{1\text{D}}/c_s < 9.5$  and  $\sigma_{1\text{D}}/c_s < 13$ , respectively, and where

$$\sigma_{1\text{D}} \equiv \left(\frac{\iiint_{r < r_{\text{crit}}} \rho \delta v_r^2 dV}{\iiint_{r < r_{\text{crit}}} \rho dV}\right)^{1/2} \quad (11)$$

is the mass-weighted one-dimensional velocity dispersion of a core. An important point to note is that Equations (9) and (10) do not simply substitute  $c_s^2 \rightarrow c_s^2 + \sigma_{1\text{D}}^2$  in Equations (1) and (2), but rather, there are different functional dependences on turbulent and thermal velocities.<sup>2</sup>

We note that from the definitions in Equation (3) and Equation (11), the internal velocity dispersion, core radius, and sonic radius at the critical time are related by

$$\frac{\sigma_{1\text{D}}}{c_s} = a \left(\frac{3}{2p+3}\right)^{1/2} \left(\frac{r_{\text{crit}}}{r_s}\right)^p, \quad (12)$$

where  $a$  is almost constant at  $a \approx 0.9$ , with very weak dependence on  $p$  and  $\sigma_{1\text{D}}$ . Thus, trans-sonic cores with  $p \sim 1/3 - 1/2$  have  $r_{\text{crit}}/r_s \sim 1$ .

For a given power law index  $p$ , the TES solutions show that critical cores have a dimensionless sonic radius  $\xi_s$

<sup>2</sup> For the high-turbulence regime  $\sigma_{1\text{D}}/c_s \gtrsim 10$ , a better fit replaces  $0.5(\sigma_{1\text{D}}/c_s)^2$  in both relations by  $0.16(\sigma_{1\text{D}}/c_s)^{2.5}$ . However, this regime is not relevant to the critical cores found in our simulations.

(see Equation (4) for definition) that monotonically decreases with increasing  $\sigma_{1\text{D}}/c_s$  (see Figure 4(d) of Paper I). For  $p = 0.5$ , we find that an approximate relation

$$\xi_s \approx 2.42 + 4 \left(\frac{\sigma_{1\text{D}}}{c_s}\right)^{-2}, \quad (13)$$

holds within a relative error of 1.85% for  $\sigma_{1\text{D}} < 10c_s$ .

If a core with critical radius  $r_{\text{crit}}$  (based on its central density) and velocity dispersion  $\sigma_{1\text{D}}$  is in a state of turbulent quasi-equilibrium, with a linewidth–size index  $p = 0.5$ , Equations (1) and (9) imply that its average density within  $r_{\text{crit}}$  would be approximately

$$\bar{\rho}_{\text{TES}} \equiv 0.581 \frac{c_s^2}{Gr_{\text{crit}}^2} \left(1 + 0.5 \frac{\sigma_{1\text{D}}^2}{c_s^2}\right)^{2/3}. \quad (14)$$

This can be regarded as a prediction of the TES theory relating the radius, mean density, and velocity dispersion of critical cores. As a generalization of the classical BE relation, the prediction in Equation (14) can be compared to both simulations (as we shall do in this paper) and to observations.

The initial setup of the turbulent cloud simulations conducted in Paper II consists of uniform density in a periodic box of side length  $L_{\text{box}}$ , with turbulent velocity perturbations randomly initialized from a Gaussian distribution with a  $k^{-2}$  power spectrum (corresponding to a linewidth–size relation  $\Delta v(l) \propto l^{1/2}$ ). We adopt an isothermal equation of state with

$$c_s = 0.188 \text{ km s}^{-1} \left(\frac{T}{10 \text{ K}}\right)^{1/2}, \quad (15)$$

assuming  $\mu = 2.3m_{\text{H}}$  appropriate for 10% helium abundance by number. Apart from the dependence on a random seed, the initial conditions are fully specified with the two dimensionless parameters: the number of Jeans lengths initially contained in the domain,  $L_{\text{box}}/L_{J,0}$ , and the root-mean-square Mach number  $\mathcal{M}_{3\text{D}}$  averaged within the cubic volume  $L_{\text{box}}^3$ . Here,

$$L_{J,0} \equiv \left(\frac{\pi c_s^2}{G\rho_0}\right)^{1/2} = 1.93 \text{ pc} \left(\frac{T}{10 \text{ K}}\right)^{1/2} \left(\frac{n_{\text{H},0}}{200 \text{ cm}^{-3}}\right)^{-1/2} \quad (16)$$

is the Jeans length at the cloud’s average density  $\rho_0 = 1.4m_{\text{H}}n_{\text{H},0}$ . The corresponding mass and time scales are the Jeans mass

$$M_{J,0} \equiv \rho_0 L_{J,0}^3 = 49.9 M_{\odot} \left(\frac{T}{10 \text{ K}}\right)^{3/2} \left(\frac{n_{\text{H},0}}{200 \text{ cm}^{-3}}\right)^{-1/2} \quad (17)$$

and the Jeans time

$$t_{J,0} \equiv \frac{L_{J,0}}{c_s} = 10.0 \text{ Myr} \left(\frac{n_{\text{H},0}}{200 \text{ cm}^{-3}}\right)^{-1/2}, \quad (18)$$

which is related to the cloud’s free-fall time

$$\begin{aligned} t_{\text{ff},0} &\equiv \left( \frac{3\pi}{32G\rho_0} \right)^{1/2} = 0.306t_{J,0} \\ &= 3.08 \text{ Myr} \left( \frac{n_{\text{H},0}}{200 \text{ cm}^{-3}} \right)^{-1/2}. \end{aligned} \quad (19)$$

In [Paper II](#), we conducted 40 simulations with  $\mathcal{M}_{3\text{D}} = 5$  (model M5) and 7 simulations with  $\mathcal{M}_{3\text{D}} = 10$  (model M10), by varying the random seed for the initial cloud turbulence. The box sizes for model M5 and M10 are set to  $L_{\text{box}} = 2L_{J,0}$  and  $4L_{J,0}$ , respectively, to fix the cloud-scale virial parameter at

$$\alpha_{\text{vir}} \equiv \frac{5c_s^2 \mathcal{M}_{3\text{D}}^2 R_{\text{box}}}{3GM_{\text{box}}} = 2.06, \quad (20)$$

where  $M_{\text{box}} = L_{\text{box}}^3 \rho_0 \equiv 4\pi R_{\text{box}}^3 \rho_0 / 3$  is the total mass and  $R_{\text{box}} = [3/(4\pi)]^{1/3} L_{\text{box}} \approx 0.62L_{\text{box}}$  is an effective spherical radius. The chosen box size and Mach number set the average sonic radius,

$$r_{s,\text{cloud}} \equiv \frac{9}{8} \frac{L_{\text{box}}}{\mathcal{M}_{3\text{D}}^2} = 0.645L_{J,0} \alpha_{\text{vir}}^{-1/2} \mathcal{M}_{3\text{D}}^{-1}, \quad (21)$$

at which turbulent velocity dispersion following the cloud’s mean linewidth–size relation equals the sound speed; the factor 9/8 accounts for the conversion between three-dimensional volume-average  $\mathcal{M}_{3\text{D}}$  and one-dimensional shell-average  $\langle \delta v_r^2 \rangle_\rho^{1/2}$  (see [Equation \(49\)](#) and related text in [Paper II](#)).

Cores that develop in simulations have densities comparable to the post-shock value at the global Mach number of the cloud,  $\rho \sim \rho_{\text{ps}} = \mathcal{M}_{3\text{D}}^2 \rho_0$ . [Equation \(21\)](#) thus indicates that, for realistic clouds with  $\alpha_{\text{vir}} \gtrsim 2$ , resolving the sonic radius in ambient gas poses a similar challenge to resolving dense cores, which have typical sizes on the order of  $R_{\text{BE}}(\rho_{\text{ps}}) = 0.430L_{J,0} \mathcal{M}_{3\text{D}}^{-1}$ . In order to have  $r_{s,\text{cloud}}$  sufficiently resolved and also have cores resolved down to a mass  $M_{\text{BE}}(2\rho_{\text{ps}})$  we set the number of cells per dimension  $N = 1024$  for model M10 and  $N = 512$  for M5 (see [Section 3.3](#) of [Paper II](#) for details on the resolution requirements). The resulting cell size normalized to the average Jeans length is  $\Delta x/L_{J,0} = (L_{\text{box}}/N)/L_{J,0} = 3.91 \times 10^{-3}$  for both models.

We consider a self-gravitating core with radius  $r_{\text{crit}}$  resolved if

$$r_{\text{crit}} > N_{\text{core,res}} \Delta x, \quad (22)$$

where our standard choice is  $N_{\text{core,res}} = 8$  unless otherwise mentioned. We note that this is a conservative choice amounting to resolving a core volume with  $4\pi N_{\text{core}}^3/3 = 2145$  resolution elements. A core would still be marginally resolved with less restrictive choice

of  $N_{\text{core,res}} = 4$ . Given that the radius of the smallest resolvable core would be  $R_{\text{BE}} = N_{\text{core,res}} \Delta x$ , one can use the corresponding BE mass to derive the minimum resolvable mass:

$$M_{\text{min}} = 2.43 \frac{c_s^2}{G} N_{\text{core,res}} \Delta x. \quad (23)$$

For simulations adopting a fixed mass resolution  $\Delta m$ , the equivalent minimum resolvable mass may be written as

$$M_{\text{min}} = \frac{4\pi N_{\text{core,res}}^3}{3} \Delta m. \quad (24)$$

As described in [Section 1](#), in [Paper II](#) we directly identify the critical time of individual simulated cores by measuring the net radial force  $F_{\text{net}}$  over time within these cores. Because cores would be persistently accelerated toward the center during gravitational runaway, we define the critical time  $t_{\text{crit}}$  by

$$t_{\text{crit}} \equiv \min \{ t^* \mid F_{\text{net}}(r_{\text{crit}}) < 0 \forall t \in (t^*, t_{\text{coll}}) \}. \quad (25)$$

That is, the net radial force  $F_{\text{net}}(r_{\text{crit}})$  acting on a ball of radius  $r_{\text{crit}}$  becomes negative at  $t_{\text{crit}}$  and stays negative until the end of the collapse at  $t_{\text{coll}}$  (see [Equation \(60\)](#) of [Paper II](#) for the radial equation of motion that relates  $F_{\text{net}}$  to radial acceleration). For the collapse time of each core, we use the following working definition:

$$t_{\text{coll}} \equiv \text{The time of each sink particle formation.} \quad (26)$$

The duration of collapse for each core is then defined by

$$\Delta t_{\text{coll}} \equiv t_{\text{coll}} - t_{\text{crit}}, \quad (27)$$

which can be measured for individual cores. Note that [Equations \(25\)](#) and [\(26\)](#) provide quantitative definition of the critical time and the collapse time described in [Section 1](#).

### 3. PROPERTIES OF CRITICAL CORES

In this section, we present an analysis of the physical properties of all resolved cores in models M5 and M10, measured at the critical time  $t_{\text{crit}}$  defined in [Equation \(25\)](#). For convenience, we use the term “critical core” to denote a ball of radius  $r_{\text{crit}}$  at  $t = t_{\text{crit}}$ . The radius and mass of critical cores are then defined by

$$R_{\text{core}} \equiv r_{\text{crit}}, \quad (28)$$

$$M_{\text{core}} \equiv \iiint_{r < R_{\text{core}}} \rho dV, \quad (29)$$

where all quantities are evaluated at  $t = t_{\text{crit}}$  for each core.

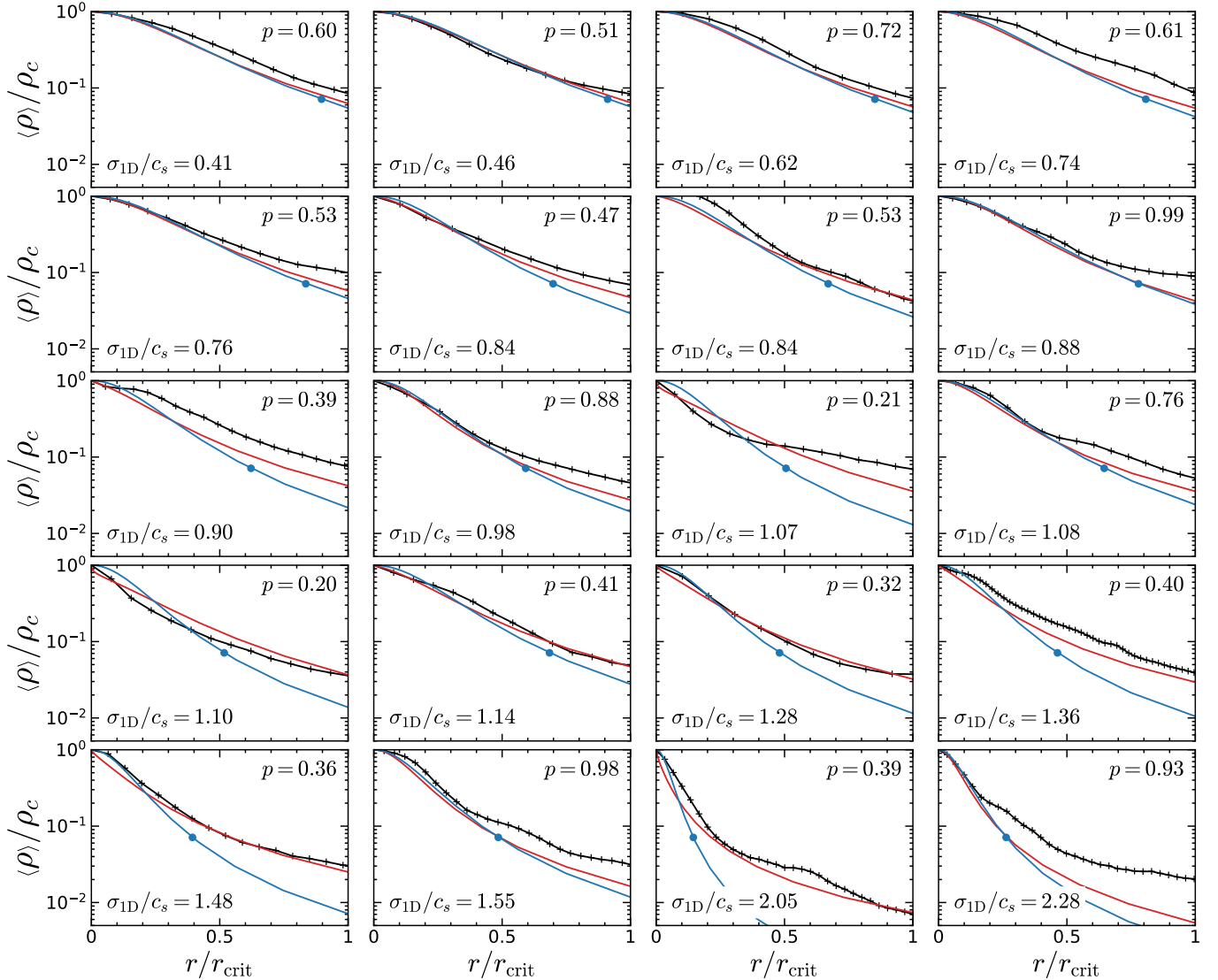


**Figure 1.** Radial density profiles of 20 randomly selected critical cores in model M10, arranged in an increasing order of  $\sigma_{1D}$  from left to right and top to bottom. In each panel, the black line with markers plots the measured density profile while the red line shows the analytic equilibrium solution of the critical TES constructed from the measured  $\rho_c$ ,  $r_s$ , and  $p$  (i.e., the red line is not a fit to the black line). For comparison, we also plot the similar profile of the BE sphere in the blue line using the measured  $\rho_c$  but assuming only thermal pressure (i.e.  $r_s \rightarrow \infty$ ). The blue circle marks the location of  $R_{\text{BE}}$ . In each panel, the density and radius are normalized by  $\rho_c$  and  $R_{\text{core}} = r_{\text{crit}}$ , respectively. The mass-weighted average velocity dispersion  $\sigma_{1D}$  and the power-law index of the fitted linewidth–size relation  $p$  are annotated in each panel.

### 3.1. Radial Density Profiles

Figure 1 plots the normalized radial density profiles measured at  $t = t_{\text{crit}}$ , for 20 randomly selected cores in model M10. For comparison, we also plot the theoretical TES and BE solutions obtained using the measured central density  $\rho_c$ , sonic radius  $r_s$ , and power law index  $p$  (for the BE sphere, we assume  $r_s \rightarrow \infty$ ). The latter two quantities are obtained by fitting Equation (3) to the measured profile of  $\langle \delta v_r^2 \rangle_\rho^{1/2}$ , within the tidal radius defined by the distance to the nearest saddle point of the gravitational potential (see Paper II). Figure 1

indicates that while the measured profiles are broadly consistent with the TES solutions, they cannot be described by BE spheres unless  $\sigma_{1D}$  (see Equation (11) for definition) is small compared to  $c_s$  or the linewidth–size index  $p$  (see Equation (3)) is large. For the cases with supersonic turbulence within a core, density decreases at large radii much less in the simulated cores (and in the TES solutions) than in the BE solutions that match the profiles at small radius. Some cores do show moderate discrepancies from TES profiles for one or a combination of the following reasons: Departure from the spher-

ical symmetry or the presence of nearby structures that make the gravitational force deviate from  $GM/r^2$ ; traveling shock waves that intermittently throw a core out of equilibrium; strong converging flows building a core in less than a sound crossing time (we come back to this in Figure 10); non-negligible rotation; a linewidth–size relation which does not conform to a single power law. Nonetheless, the overall agreement between radial density profiles of the simulated cores and TES solutions suggests that quasi-steady equilibrium structures supported by thermal and turbulent pressures naturally emerge from the interplay between supersonic turbulence and self-gravity.

### 3.2. Local Linewidth–size Relations and Correlation with Density

The comparison in Figure 1 suggests that turbulence affects density structure and stability to varying extents across different cores. In this section, we demonstrate how the local variations of the turbulent scaling relation affect the critical density at which collapse is triggered. To illustrate the variations in the locally-constructed linewidth–size relations, in Figure 2(a) we plot the turbulent velocity dispersion  $\langle \delta v_r^2 \rangle_\rho^{1/2}$  measured for each critical core as a function of growing radius from the core center (see Equation (3)). The colors show the ratio  $r_s/r_{s,\text{cloud}}$ , i.e., the local sonic radius relative to the cloud average defined in Equation (21). Figure 2(a) shows that the turbulent velocity dispersion measured at a given size scale varies up to a factor of a few above and below the average relation given by  $c_s(r/r_{s,\text{cloud}})^{0.5}$ . Alternatively, it implies that the locally measured sonic radius,  $r_s$ , exhibits order of magnitude variations around  $r_{s,\text{cloud}}$ .

Large spatial variations in the strength of turbulence shown in Figure 2(a) suggest that the necessary density for cores to collapse would differ considerably from core to core. Figure 2(b) plots the density profiles of critical cores normalized to the average cloud density  $\rho_0$  and the associated Jeans length  $L_{J,0}$ , with the same color coding as in Figure 2(a). The noticeable vertical color gradients suggest that cores forming in more turbulent regions (i.e., smaller  $r_s$ ) overall have higher densities when compared at a given radius.

To illustrate this point more clearly, in Figure 3 we plot the central density  $\rho_c$  versus the local sonic radius  $r_s$  for all critical cores in models M5 and M10. It shows that, for critical cores,  $r_s$  and  $\rho_c$  are anticorrelated, meaning that cores in regions of strong turbulence need to reach higher densities to initiate collapse. The distribution shown in Figure 3 also exhibits scatter in the direction perpendicular to the overall anticorre-

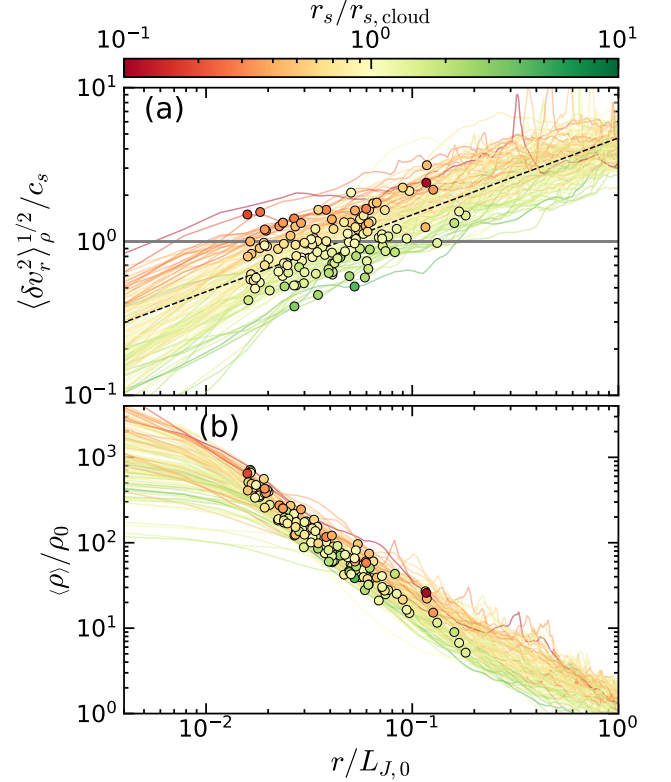


**Figure 2.** Radial profiles of (a) turbulent velocity dispersion and (b) density, for the critical cores in model M10. Individual lines correspond to the profiles constructed starting from the center of each core, where we include the cores with  $r_{\text{crit}} \geq 4\Delta x$  (i.e.,  $N_{\text{core,res}} = 4$ ). The critical radius  $r_{\text{crit}}$  is marked with circles. The black dashed line in panel (a) plots the average linewidth–size relation,  $\langle \delta v_r^2 \rangle_\rho^{1/2} / c_s = (r / r_{s,\text{cloud}})^{0.5}$ , where the colors represent the ratio of the local sonic radius  $r_s$  to the average  $r_{s,\text{cloud}}$  (i.e., the local deviations from the mean turbulent scaling relation). The intersection points between each colored line and the horizontal gray line representing  $\langle \delta v_r^2 \rangle_\rho^{1/2} / c_s = 1$  correspond to the local sonic radius  $r_s$  for each core.

lation, which, together with the overall anticorrelation, can be understood in the framework of TESs as follows.

Assuming  $p = 0.5$ , Equations (4) and (13) yield an expression for the central density required for a core to collapse, relative to the cloud’s average density, depending on its level of turbulence:

$$\frac{\rho_c}{\rho_0} \approx \frac{1}{4\pi^2} \left( \frac{r_s}{L_{J,0}} \right)^{-2} \left[ 2.42 + 4 \left( \frac{\sigma_{1D}}{c_s} \right)^{-2} \right]^2. \quad (30)$$

We note that the term in the square bracket can be alternatively expressed by  $2.42 + 6.6r_s/r_{\text{crit}}$ , using Equation (12) with  $a = 0.9$  and  $p = 0.5$ . Thus, Equation (30) indicates that  $\rho_c$  is overall proportional to  $r_s^{-2}$ , with scatter from varying  $\sigma_{1D}/c_s$  modulated by relative core

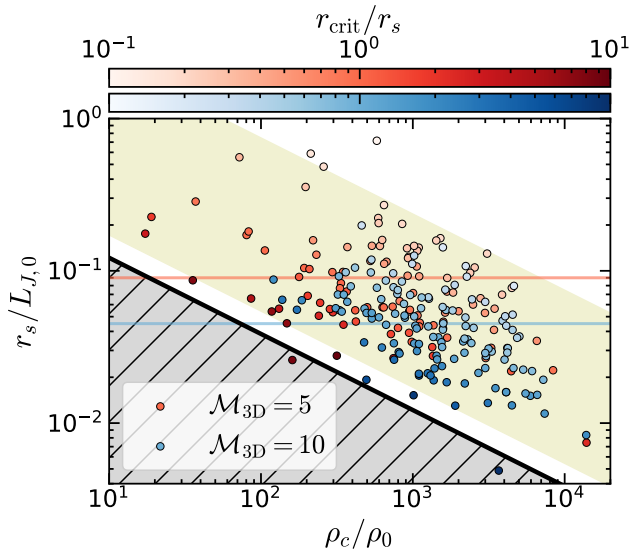


**Figure 3.** Local sonic radius versus central density measured for selected individual cores from model M5 (red) and M10 (blue), satisfying the resolution criterion  $N_{\text{core,res}} = 4$ . Black line plots Equation (31), such that a TES with  $p = 0.5$  is stable at all radii when  $r_s$  and  $\rho_c$  falls in the gray shaded region. Horizontal red and blue lines correspond to  $r_{s,\text{cloud}}$  (defined in Equation (21)) for model M5 and M10, respectively. Circles are colored by  $r_{\text{crit}}/r_s$ , where  $\sigma_{1\text{D}}/c_s \approx 0.8(r_{\text{crit}}/r_s)^{1/2}$  from Equation (12). The yellow shaded band is the region where  $\sigma_{1\text{D}}/c_s$  is between 0.3 (upper edge) and 2 (lower edge).

size  $r_{\text{crit}}/r_s$ , consistent with the trend observed in Figure 3. At fixed  $r_s$ , larger and more turbulent cores (which go together following  $\sigma_{1\text{D}}/c_s \approx 0.8(r_{\text{crit}}/r_s)^{1/2}$ ) have lower  $\rho_c/\rho_0$ . As emphasized in Paper I and Paper II, core size is subject to the local gravitational potential environment.

It is worth noting that almost all critical cores fall under the region of parameter space where  $\sigma_{1\text{D}}/c_s \in [0.3, 2]$  (shown as yellow shaded band in Figure 3). That is, we find neither purely thermal cores with  $\sigma_{1\text{D}} \ll c_s$ , nor highly turbulent cores with  $\sigma_{1\text{D}} \gg c_s$ . The center of the distribution shown in Figure 3 lies roughly along  $\xi_s \sim 9$ , corresponding to  $\sigma_{1\text{D}}/c_s = 0.78$ . For a  $p = 0.5$  TES, the critical radius becomes identical to the sonic radius when  $\xi_s \sim 9$  (see Figure 4(a) of Paper I). This means that cores in our simulations on average have  $r_{\text{crit}} \sim r_s$  at the onset of collapse. We discuss physical reasons for this below.

Paper II found that collapse occurs when  $r_{\text{crit}}$  decreases below the tidal radius  $r_{\text{tidal}}$ , which is set by local geography of the gravitational potential. Our results therefore imply that critical cores generally satisfy  $r_{\text{crit}} \sim r_s \sim r_{\text{tidal}}$ . Indeed,  $r_s$  is the scale at which the nonlinear structures are expected, which may in turn de-

termine the size of the local potential well characterized by  $r_{\text{tidal}}$ .

We additionally note that, for a given  $r_s$ , there exists a minimum central density below which all TES solutions are stable (Paper I). For  $p = 0.5$ , this minimum can be obtained by taking the  $\sigma_{1\text{D}} \rightarrow \infty$  limit in Equation (30), leading to

$$\frac{\rho_{c,\text{min}}}{\rho_0} = 0.148 \left( \frac{r_s}{L_{J,0}} \right)^{-2} \quad (31)$$

This is plotted in a solid black line in Figure 3. In the presence of turbulence satisfying Equation (3) with  $p = 0.5$ , the theory predicts that collapse cannot occur in the shaded region below this borderline. The absence of critical cores from our simulations in the shaded region is consistent with this theoretical prediction. As shown in Figure 17 of Paper II, cores generally form in this stable regime and then evolve diagonally through the borderline, until the critical conditions are satisfied at various locations within the yellow shaded region of the parameter space shown in Figure 3.

### 3.3. Distribution of Turbulence Parameters and Core Densities

Figure 4 plots the distribution of  $p$ ,  $r_s$ ,  $\xi_s$ , and  $\sigma_{1\text{D}}$  from all critical cores in models M5 and M10. The median values of  $p$  (the index of the fitted linewidth–size relation in Equation (3)) are 0.43 and 0.58 for model M5 and M10, respectively, roughly consistent with the expected average slope of 0.5 resulting from the initial velocity power spectrum. However, the distribution is rather broad, such that individual cores can have diverse values of  $p$  ranging between  $\sim 0.2$ – $0.8$ . Cores in model M5 have overall slightly smaller values of  $p$  compared to those forming in model M10.

Due to higher initial  $\mathcal{M}_{3\text{D}}$ , the sonic radius of the cores is generally smaller in model M10. The median values are  $r_s = 8.9 \times 10^{-2} L_{J,0}$  and  $5.0 \times 10^{-2} L_{J,0}$  for model M5 and M10, respectively, entirely consistent with what expected from the initial box-scale Mach number (Equation (21)).<sup>3</sup>

While cores in model M10 have overall smaller  $r_s$  than model M5, they tend to have higher  $\rho_c$ , presumably due to the stronger turbulent compression of core-forming regions at higher cloud-scale Mach number. This makes the distribution of the dimensionless sonic radius  $\xi_s = (4\pi G \rho_c)^{1/2} r_s / c_s$  (which determines the

<sup>3</sup> Although the box-averaged Mach number has decayed from its initial  $\mathcal{M}_{3\text{D}}$  by the time most cores form and collapse, we find the energy loss is predominantly at large scales and the velocity structure function at core scales is in fact consistent with the initial condition (see Figure 2(a) as well as Figure 16 of Paper II).



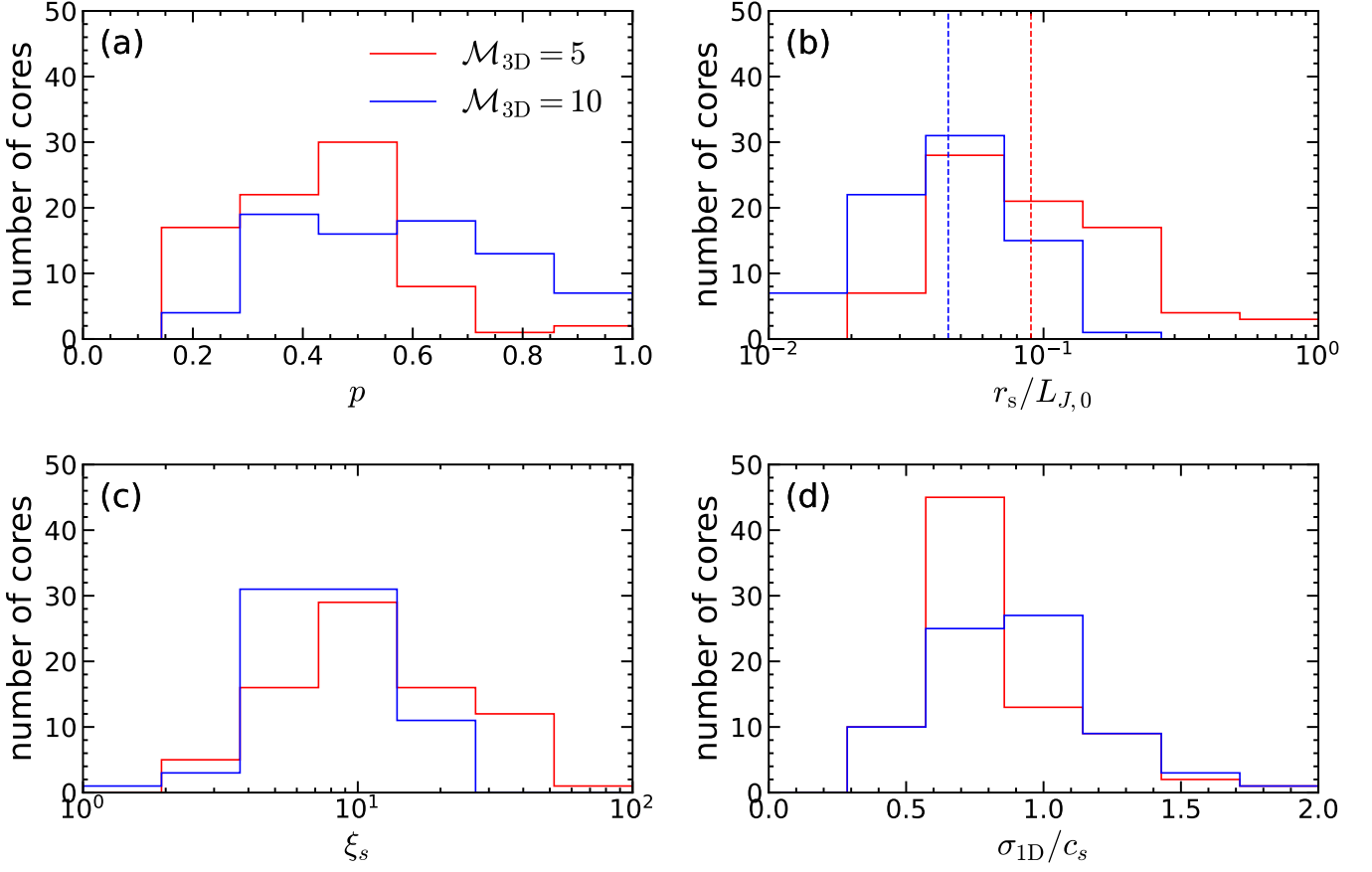


**Figure 4.** Distributions of dynamical properties in all critical cores from models M5 (red) and M10 (blue). Shown are (a) the power-law exponent  $p$  of the linewidth–size relation, (b) the sonic radius  $r_s$ , (c) the dimensionless sonic radius  $\xi_s$  (see Equation (4)), and (d) the mass-weighted average velocity dispersion  $\sigma_{1D}$  (Equation (11)). The vertical dotted lines in panel (b) mark the initial sonic radius  $r_{s,\text{cloud}}$  defined in (Equation (21)) which is expected from the large-scale  $k^{-2}$  velocity power spectrum.

structure of forming cores; see Paper I) not very different between models M5 and M10. The median and  $\pm 34.1$ th percentile range of  $\xi_s$  for the entire ensemble of cores is  $9.1^{+9.8}_{-4.2}$ .

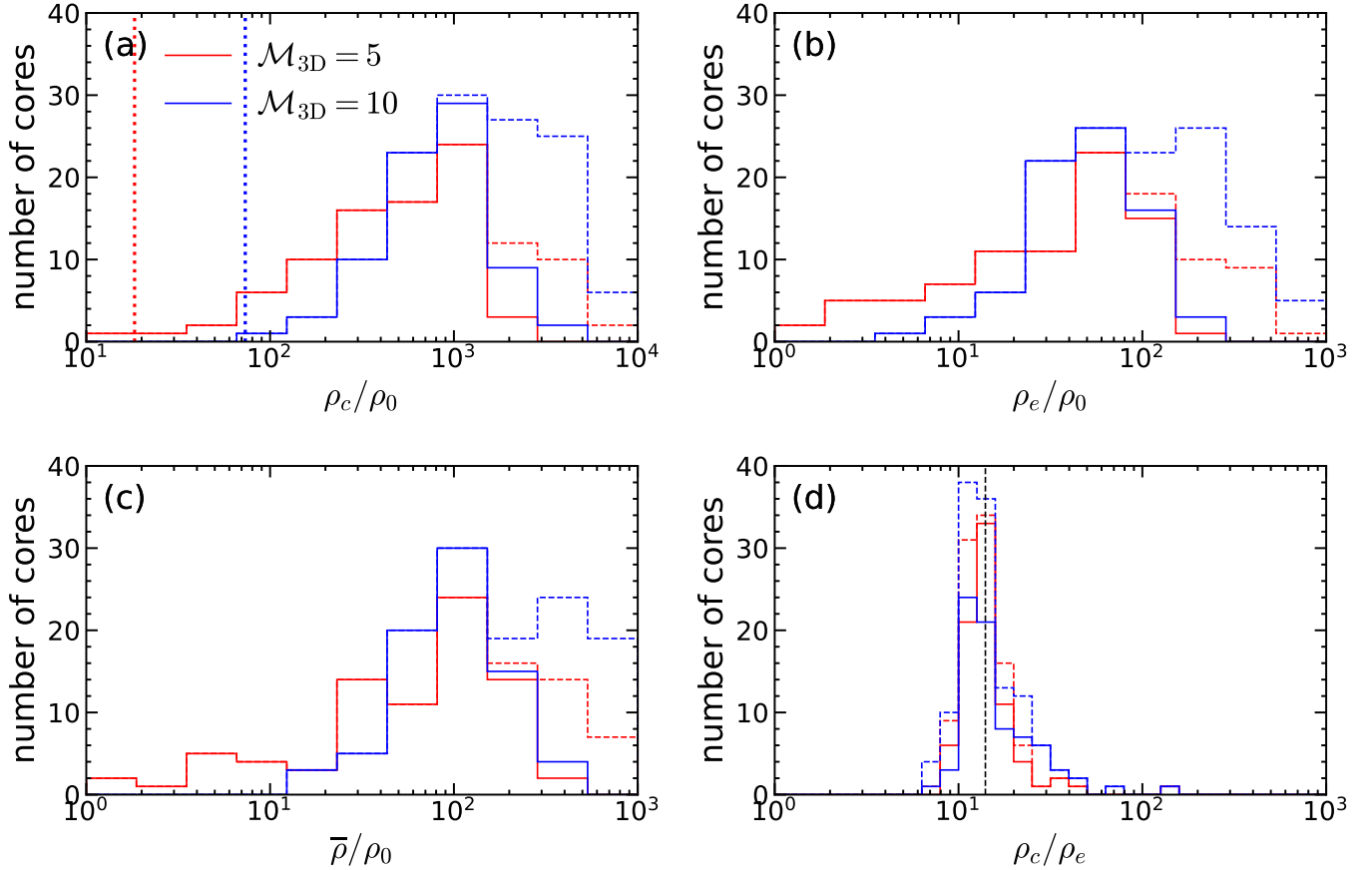
Figure 4(d) shows that most cores in models M5 and M10 have subsonic or transonic velocity dispersions, as noted in connection to Figure 3. The level of turbulence in our critical cores is consistent with the kinematics of observed prestellar cores (e.g., Lee et al. 1999, 2001; Foster et al. 2009; Friesen et al. 2009, 2010; Lee et al. 2014; Storm et al. 2016; Kirk et al. 2017; Tang et al. 2018; Chen et al. 2019; Kerr et al. 2019; Choudhury et al. 2021; Li et al. 2023). The median and  $\pm 34.1$ th percentile range of  $\sigma_{1D}/c_s$  is  $0.79^{+0.38}_{-0.21}$ .

Figure 5 plots the distribution of densities of cores at their critical time: Central  $\rho_c$ , edge  $\rho_e$  (defined as the value at  $r = R_{\text{core}}$ ), and mean  $\bar{\rho} = M_{\text{core}}/(4\pi R_{\text{core}}^3/3)$ , as well as the center-to-edge contrast  $\rho_c/\rho_e$ . This makes clear that cores form at a wide range of densities, with a typical value around  $\bar{\rho} \sim 10^2 \rho_0$ , corresponding to

$\bar{n}_{\text{H}_2} \sim 10^4 \text{ cm}^{-3}$  for a cloud with average molecular hydrogen number density  $n_{\text{H}_2,0} = 10^2 \text{ cm}^{-3}$ . A caveat is that the distribution is likely to become incomplete somewhere in the regime  $\bar{\rho}/\rho_0 \gtrsim 10^2\text{--}10^3$ ; we refer the reader to Section 3.3 of Paper II for a discussion of our resolution criteria. The distribution of center-to-edge density contrast is narrow, peaking at  $\rho_c/\rho_e \sim 10\text{--}30$ . Some cores have a center-to-edge contrast of less than 14 because they have excess mass at their edge compared to isolated TES solutions (e.g., Figure 1).

It is interesting to reexamine the distribution of  $\rho_c$  in models M5 and M10 by using Equation (30). Neglecting the local variations of  $r_s$  and instead adopting the “average” value  $r_s = r_{s,\text{cloud}}$  defined in Equation (21), one can relate the required central density to a cloud’s virial parameter and Mach number as

$$\frac{\rho_c}{\rho_0} \approx 6.08 \times 10^{-2} \left[ 2.42 + 4 \left( \frac{\sigma_{1D}}{c_s} \right)^{-2} \right]^2 \alpha_{\text{vir}} \mathcal{M}_{3D}^2, \quad (32)$$



**Figure 5.** Distribution of density values in all critical cores from models M5 (red) and M10 (blue), satisfying the resolution criterion (Equation (22)) with the standard choice of  $N_{\text{core,res}} = 8$  (solid histograms) and the relaxed choice  $N_{\text{core,res}} = 4$  (dashed histograms). Shown are (a) center, (b) edge, (c) mean densities relative to the mean density in the box, and (d) the center-to-edge density contrast. In (a), vertical dotted lines plot the theoretical prediction for the minimum central density allowing instability, assuming  $p = 0.5$  (Equation (33)). The vertical dotted line in the panel (d) marks  $\rho_c/\rho_e = (\rho_c/\rho_e)_{\text{BE}} = 14$ .

where an implicit assumption is  $p = 0.5$  inherited from using Equation (13). For a cloud with given  $\alpha_{\text{vir}}$  and  $\mathcal{M}_{3\text{D}}$ , Equation (32) has a lower bound,

$$\frac{\rho_{c,\text{min}}}{\rho_0} = 0.356\alpha_{\text{vir}}\mathcal{M}_{3\text{D}}^2, \quad (33)$$

in the limit of  $\sigma_{1\text{D}} \rightarrow \infty$ . For models M5 and M10, Equation (33) yields  $\rho_{c,\text{min}} = 18\rho_0$  and  $73\rho_0$ , respectively, which are intriguingly similar to the lower edges of the central density distribution shown in Figure 5(a). For transonic cores with  $\sigma_{1\text{D}} = 0.8c_s$  (representative in Figure 4(d)), Equation (32) yields  $\rho_c = 235\rho_0$  and  $941\rho_0$  for models M5 and M10, respectively, which are closer to typical central densities of cores.

### 3.4. Core Mass and Radius Distributions

Figure 6(a) plots the mass function of critical cores, defined as the number of cores per logarithmic interval of  $M_{\text{core}}$ , for models M5 and M10. We introduce a new term “critical core mass function” (CCMF) to distinguish our

mass function, which is specifically constructed at  $t_{\text{crit}}$  of each core, from observed CMFs consisting of cores at various evolutionary stages. We also plot the distribution of the core radius in Figure 6(b). We remind the reader that these cores are defined at their own critical time, which occurs at a different point in the simulation for each core. Although the CCMF shows marginal evidence of a peak, the location of a peak is only a factor of  $\sim 2$  higher than  $M_{\text{min}}/M_{J,0} = 2.42 \times 10^{-2} (N_{\text{core,res}}/8)$  if we adopt  $N_{\text{core,res}} = 8$  in Equation (23), requiring some caution in interpretation. If we relax the criterion for cores being resolved from  $N_{\text{core,res}} = 8$  to 4, the nominal resolved mass drops to  $M_{\text{min}}/M_{J,0} = 1.21 \times 10^{-2}$ . While the CCMF peak position for model M5 does not vary much after including these lower mass cores, the peak shifts toward lower mass for model M10. We note, however, that at higher resolution, turbulent dissipation would have been lower in these less resolved cores and they would have been prevented from collapsing.

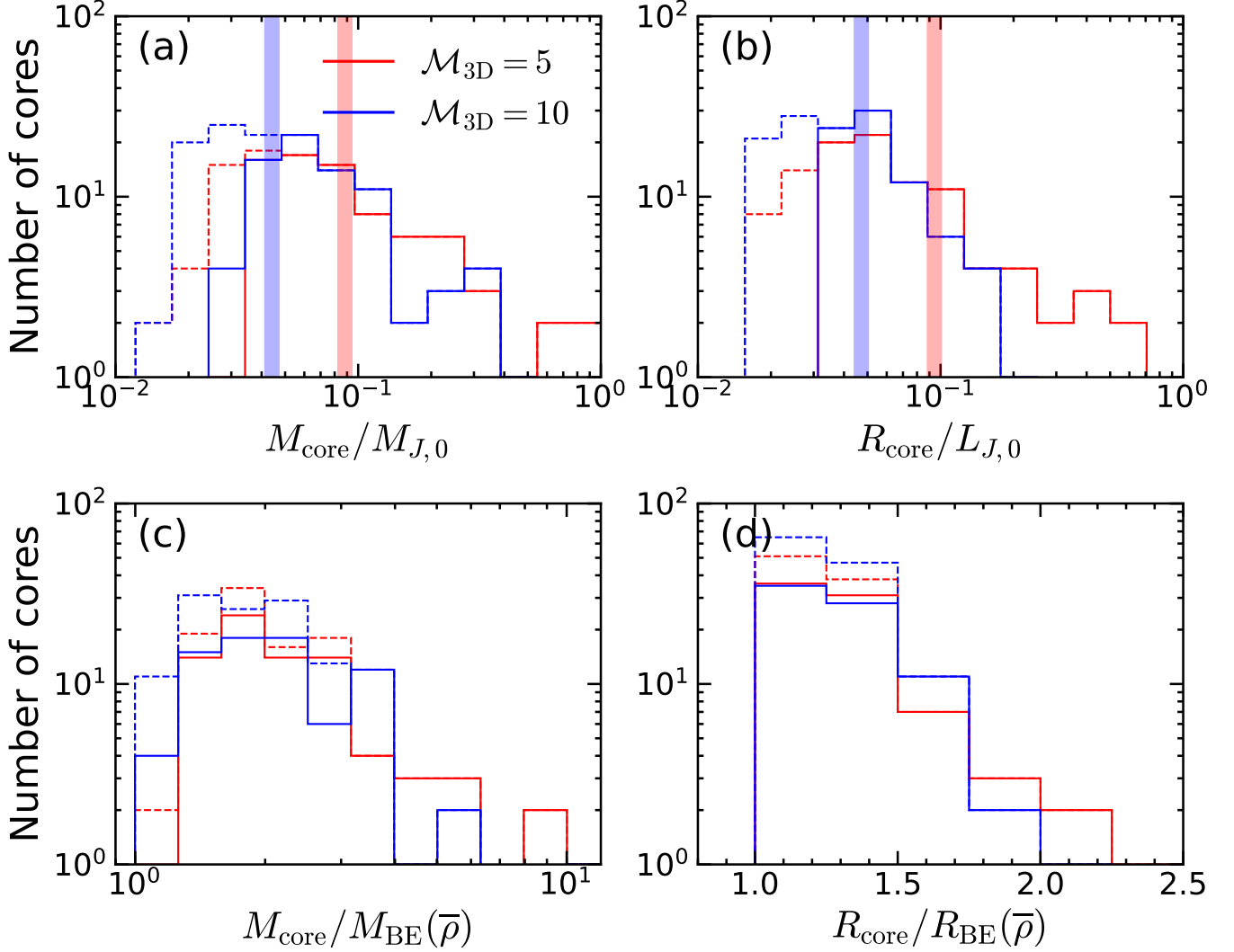


**Figure 6.** Distribution of mass and radius of critical cores in models M5 (red) and M10 (blue), satisfying the resolution criterion (Equation (22)) with the standard choice of  $N_{\text{core, res}} = 8$  (solid histograms) and the relaxed choice  $N_{\text{core, res}} = 4$  (dashed histograms). (a) The CCMF; bin lower limits for mass are at  $M_{\text{min}}$  from Equation (23) for a chosen  $N_{\text{core, res}}$ . (b) The distribution of core radius, where by definition  $R_{\text{core}} = r_{\text{crit}}$  at  $t = t_{\text{crit}}$ . Lower limits are at  $N_{\text{core, res}} \Delta x$ . For (a) and (b) shaded bands mark  $M_{\text{char, trb}}$  and  $R_{\text{char, trb}}$  defined in Equation (35) and Equation (36) for  $\mathcal{M}_{3\text{D}} = 5$  and 10, respectively (see text for details). (c) The distribution of the ratio between the core mass and the BE mass evaluated at the average core density. (d) The distribution of the ratio between the core radius and the BE radius evaluated at the average core density.

If cores were supported only by thermal pressure, one might expect a characteristic mass for collapse in a turbulent simulation to be given by the BE mass in Equation (2) when  $\bar{\rho}$  is set equal to the characteristic post-shock value based on the large scale Mach number in the cloud,

$$M_{\text{char, th}} = 1.86 \frac{c_s^3}{G^{3/2} \rho_0^{1/2} \mathcal{M}_{3\text{D}}} = 0.334 \frac{M_{J,0}}{\mathcal{M}_{3\text{D}}} \quad (34)$$

(e.g. Gong & Ostriker 2011; Chen & Ostriker 2014; Haugbølle et al. 2018). Allowing for turbulent support

of cores, this would be generalized to

$$\begin{aligned} M_{\text{char, trb}} &\equiv M_{\text{crit}}(\bar{\rho} = \rho_0 \mathcal{M}_{3\text{D}}^2) \\ &\approx 0.334 \frac{M_{J,0}}{\mathcal{M}_{3\text{D}}} \left( 1 + 0.5 \frac{\sigma_{1\text{D}}^2}{c_s^2} \right) \end{aligned} \quad (35)$$

where  $M_{\text{crit}}$  is the critical TES mass including turbulent support and we use Equation (10) in the second line for  $p = 0.5$ . Taking  $\sigma_{1\text{D}} = 0.8c_s$  as a representative value in Figure 4(d), Equation (35) indicates that the characteristic mass including turbulent support is only slightly higher than the BE mass at the post-shock density given above,  $M_{\text{char, trb}} = 1.32M_{\text{char, th}}$ . For  $\mathcal{M}_{3\text{D}} = 5$

and 10, this corresponds to  $M_{\text{char, trb}} = 8.8 \times 10^{-2} M_{J,0}$  and  $4.4 \times 10^{-2} M_{J,0}$ , respectively, which are plotted in vertical shaded bands in Figure 6(a). For model M5 where the peak of the CCMF appears to be marginally resolved, the apparent peak occurs at  $\sim 0.5 M_{\text{char, trb}}$ . Scaling from this result, the expected peak position for model M10 would then be  $0.5 M_{\text{char, trb}} \sim 2.2 \times 10^{-2} M_{J,0}$ . This is close to CCMF peak for the dashed pdf, which adopts  $N_{\text{core, res}} = 4$ . However, we consider this too close to  $M_{\text{min}} = 2.42 \times 10^{-2} M_{J,0} (N_{\text{core, res}}/8)$  to be properly resolved. Both higher resolution simulations, possibly aided by adaptive mesh refinement techniques with careful refinement criteria, and extension of the parameter space to higher Mach numbers, would be required to convincingly address the questions of (1) whether or not there exists a numerically converged peak in the CCMF, and (2) whether the peak is consistent with theoretical hypotheses (see Appendix A for related discussion).

Figure 6(b) plots a similar distribution for core radius. Again, the  $\mathcal{M}_{3\text{D}} = 5$  histogram suggests that the peak in the distribution occurs at half of the characteristic radius

$$\begin{aligned} R_{\text{char, trb}} &\equiv R_{\text{crit}}(\bar{\rho} = \rho_0 \mathcal{M}_{3\text{D}}^2) \\ &\approx 0.430 \frac{L_{J,0}}{\mathcal{M}_{3\text{D}}} \left(1 + 0.5 \frac{\sigma_{1\text{D}}^2}{c_s^2}\right)^{1/3}. \end{aligned} \quad (36)$$

Figure 6(c) shows  $M_{\text{core}}$  is roughly a factor of  $\sim 2$  higher than  $M_{\text{BE}}$  measured at the average density  $\bar{\rho}$ , although a few cores have even higher ratio. While this enhancement can be attributed to turbulent support (i.e.,  $M_{\text{crit}} \geq M_{\text{BE}}$ , as in Equation (10)), some cores have additional mass excess due to rapid core building, as we will show later in Figure 10.

Finally, Figure 6(d) plots the distribution of  $R_{\text{core}}/R_{\text{BE}}$  which is equivalent to  $r_{\text{crit}}/R_{\text{BE}}$  for critical cores. It shows that the critical radius is larger than the BE radius by no more than a factor of  $\sim 2$ , which is expected for transonic cores (Equation (9)).

In Figure 7(a), we plot the ratio  $R_{\text{core}}/R_{\text{BE}}(\bar{\rho})$  as a function of the one-dimensional Mach number  $\sigma_{1\text{D}}/c_s$ . Overall, critical cores follow the curves defined by the TES solutions, although the measured ratio is slightly ( $\sim 10\%$ ) offset to higher values due to enhanced  $\bar{\rho}$  compared to strict equilibrium (Figure 7(b); we shall explain a potential reason for this in Figure 10). It is worth noting that, even though the TES model in principle extends to either a purely thermal regime with  $\sigma_{1\text{D}} \ll c_s$  or a highly turbulent regime with  $\sigma_{1\text{D}} \gg c_s$ , all of the critical cores in our simulations are found in the regime  $0.3 < \sigma_{1\text{D}}/c_s < 3$ . We find no critical cores with either very low or very high levels of internal turbulence. This is because 1) cores have a turbulent origin and are able

to initiate collapse before  $\sigma_{1\text{D}}$  completely dissipates, so that there are no purely thermal cores; 2) highly turbulent cores would be self-destructive, in the sense of being torn apart before they can collapse. In particular, Figure 8(d) of Paper I shows for TES solutions that the flow crossing time is shorter than the average free-fall time for cores with  $\sigma_{1\text{D}}/c_s > 2$ . As a result, the critical cores formed in our simulations are largely transonic, which is also likely the case for real cores.

#### 4. ACCRETION RATES AND EVOLUTIONARY STAGES

In our simulations, cores form in regions where velocity fields are locally converging. From a Eulerian perspective, the mass contained within a fixed radius  $R_{\text{core}}$  grows in time, reaching  $M_{\text{core}}$  at  $t = t_{\text{crit}}$  (see Equations (28) and (29) for definitions of  $R_{\text{core}}$  and  $M_{\text{core}}$ ). To estimate the time taken to build up  $M_{\text{core}}$  within  $R_{\text{core}}$ , we monitor the mass inflow rate

$$\dot{M}_{\text{in}} \equiv -\langle 4\pi r^2 \rho v_r \rangle = -4\pi r^2 \langle \rho \rangle \langle v_r \rangle_\rho \quad (37)$$

for each core. Figure 8(a) plots the time evolution of  $\dot{M}_{\text{in}}(r = R_{\text{core}})$  for 20 randomly selected cores, showing that the mass accretion rate is roughly constant in time, although some cores show a slightly increasing trend.

Motivated by the limited variations in  $\dot{M}_{\text{in}}$  over time, we define the duration of the core building stage as

$$\Delta t_{\text{build}} \equiv \frac{M_{\text{core}}}{\dot{M}_{\text{in}}(r = R_{\text{core}}, t = t_{\text{crit}})}. \quad (38)$$

Figure 8(c) shows that the inflow rate responsible for the core building,  $\dot{M}_{\text{in}}(r = R_{\text{core}}, t = t_{\text{crit}})$ , peaks at around  $\sim 3c_s^3/G$ . The time required to build a single BE mass core is therefore  $M_{\text{BE}}/[3c_s^3/G] \sim t_{\text{ff}}$ . Because actual core mass at  $t_{\text{crit}}$  is generally larger than  $M_{\text{BE}}$  (Figure 6(c)), the core building takes  $\Delta t_{\text{build}} \gtrsim t_{\text{ff}}$  as shown in Figure 9(a).

Also interesting is to compare the building time to the sound crossing time  $R_{\text{core}}/c_s$ . Figure 10(a) shows that most cores are built within a single sound crossing time, meaning that core building occurs dynamically rather than quasi-statically, consistent with a large scatter in the measured net force before the critical time (see Figure 12 and 15 of Paper II). Nonetheless, the core mass  $M_{\text{core}}$  measured at  $t_{\text{crit}}$  is comparable to the critical TES mass  $M_{\text{crit}}$  within a factor of  $\sim 2$  (see Figure 10(b)), indicating that most cores manage to approach a quasi-equilibrium at the end of the building stage (see also Figure 1 for radial density profiles). Interestingly, Figure 10(b) shows that the ratio  $M_{\text{core}}/M_{\text{crit}}$  increases with decreasing building time for  $\Delta t_{\text{core}} < R_{\text{core}}/c_s$ , whereas for  $\Delta t_{\text{core}} > R_{\text{core}}/c_s$

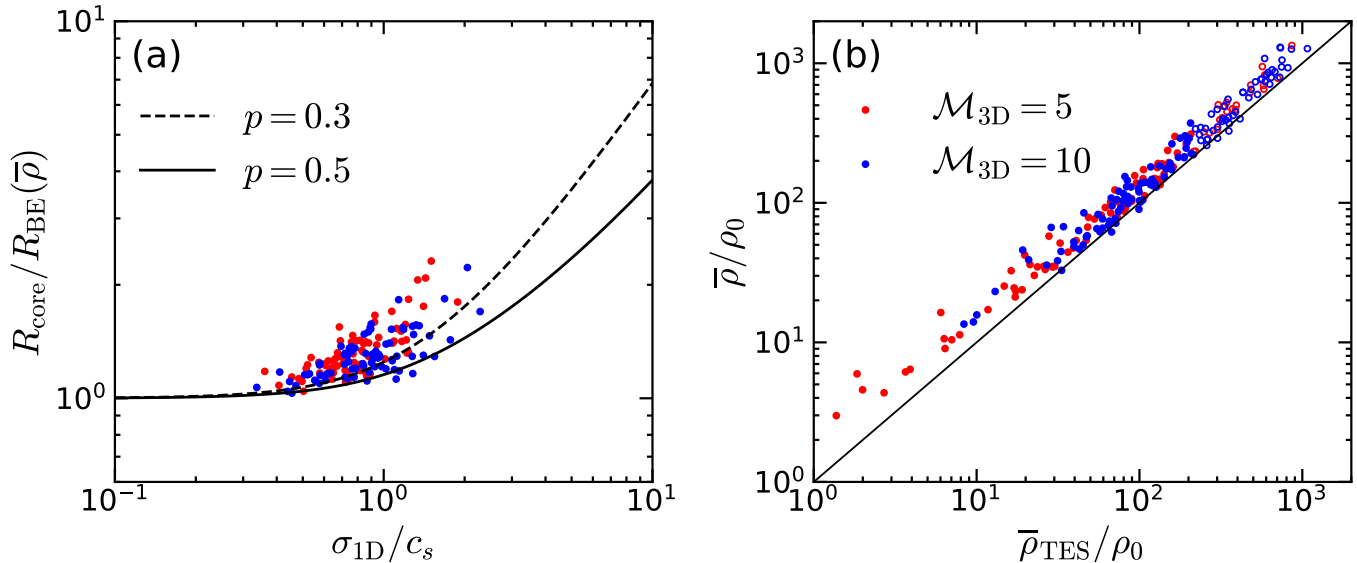


**Figure 7.** Comparison of measured core properties with TES solutions, for the critical cores in models M5 (red) and M10 (blue). (a) The ratio of the core radius to the BE radius at the average density as a function of the turbulent Mach number. The solid and dashed lines correspond to the loci of TESs with  $p = 0.5$  and  $0.3$ , respectively. (b) The average density within  $R_{\text{core}}$  versus the predicted density of  $p = 0.5$  TESs (Equation (14)). Filled and open symbols denote critical cores satisfying the resolution criterion with  $N_{\text{res,core}} = 8$  and  $4$ , respectively.

the ratio is relatively constant at  $M_{\text{core}} = 1.3M_{\text{crit}}$  (for comparison, the median ratio is  $M_{\text{core}}/M_{\text{crit}} = 1.7$  for cores with  $t_{\text{core}} < R_{\text{core}}/c_s$ ). This suggests that the cores built rapidly by strong converging flows may never go through a quasi-equilibrium configuration before collapsing; however, such cases are rare in our simulations. The dynamic nature of core building may partially explain why some cores show radial profiles deviating from the equilibrium solution (Figure 1).

To monitor the collapsing flow near the center and subsequent accretion onto the sink particle, we also measure the mass accretion rate at the center,  $\dot{M}_{\text{in}}(r \rightarrow 0)$ . We have used the notation  $\dot{M}_{\text{in}}(r \rightarrow 0)$  because, strictly speaking, the accretion rate must be formally zero at  $r = 0$ . In practice, we take  $\dot{M}_{\text{in}}(r \rightarrow 0)$  to be Equation (37) evaluated at  $r = \Delta x$  before a sink particle forms (i.e.,  $t < t_{\text{coll}}$ ), whereas we use the sink particle accretion rate defined by

$$\dot{M}_{\text{sink}}(t) \equiv \frac{M_{\text{sink}}(t) - M_{\text{sink}}(t - 10^{-3}t_{J,0})}{10^{-3}t_{J,0}} \quad (39)$$

to represent  $\dot{M}_{\text{in}}(r \rightarrow 0)$  after  $t_{\text{coll}}$ . Figure 8(b) shows that  $\dot{M}_{\text{in}}(r \rightarrow 0)$  is essentially zero before  $t_{\text{crit}}$ , while it rapidly increases as  $t \rightarrow t_{\text{coll}}$ , approaching (but not reaching) the corresponding value of the LP similarity solution,

$$\dot{M}_{\text{LP}} = 29.1 \frac{c_s^3}{G}, \quad (40)$$

although our limited output time resolution prevents us from measuring  $\dot{M}_{\text{in}}(r \rightarrow 0)$  very close to  $t_{\text{coll}}$ . We note

that the rapid increase of  $\dot{M}_{\text{in}}(r \rightarrow 0)$  does not occur immediately after  $t_{\text{crit}}$ , indicating that it takes time for the wave of outside-in collapse to reach the center.

For a centrally concentrated sphere initially at rest, it takes a central free-fall time  $t_{\text{ff},c} \equiv [3\pi/(32G\rho_c)]^{1/2}$  to form a singularity at the origin when the pressure is negligible. Figure 9(b) shows that the duration of the core collapse stage  $\Delta t_{\text{coll}}$  defined in Equation (27) is narrowly distributed around the median  $\Delta t_{\text{coll}} = 2t_{\text{ff},c}$ , indicating that the collapse monitored in our simulations is two times slower than a pressureless free-fall. We note that this is quantitatively consistent with the predicted collapse duration from the measured net force within cores (see Section 5.3 of Paper II).

After a sink particle forms at  $t_{\text{coll}}$ , the accretion rate at the center quickly declines and remains roughly constant at a level a few times smaller than  $\dot{M}_{\text{LP}}$ . This is because only the very central part of the flow manages to reach the LP asymptotic solution (Hunter 1977; Foster & Chevalier 1993; Gong & Ostriker 2009). Due to the continued accretion, the mass of a sink particle grows roughly linearly with time.

We define the time  $t_{*,100}$  as the instant at which  $M_{\text{sink}} = M_{\text{core}}$ . This time is when all the progenitor core mass has fallen to the sink (i.e., core-to-star forma-

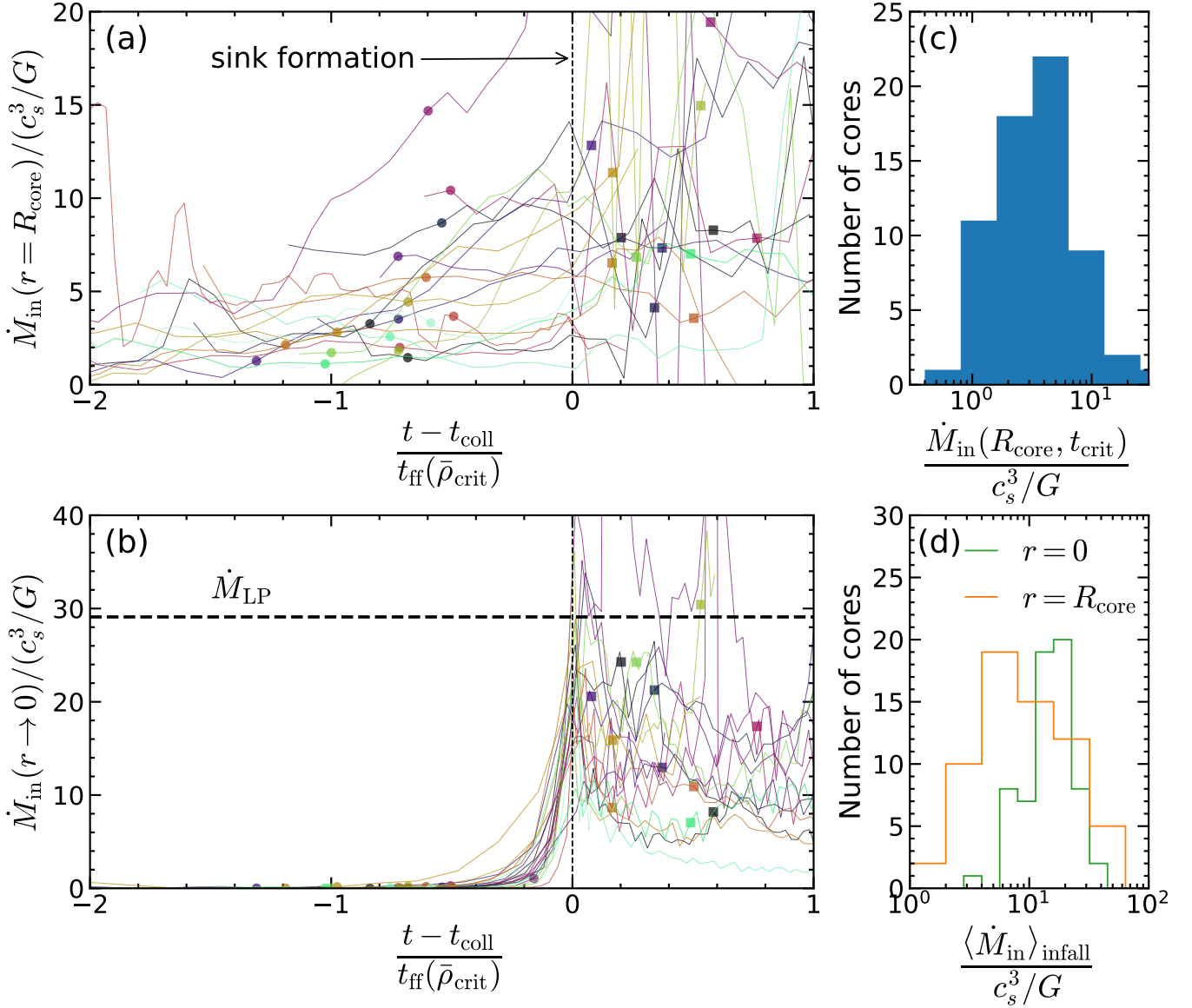


**Figure 8.** Accretion history and statistics. Left panels show temporal histories of the accretion rate for 20 randomly selected cores in model M10, measured at (a)  $r = R_{\text{core}}$  and (b)  $r = 0$  (see the main text for definitions). For each core, time is measured from  $t_{\text{coll}}$  (when a sink particle forms), such that negative (positive) time corresponds to the prestellar (protostellar) stage, and is normalized by the free-fall time at the mean core density  $\bar{\rho}_{\text{crit}} \equiv 3M_{\text{core}}/(4\pi R_{\text{core}}^3)$ . Circles and squares mark  $t_{\text{crit}}$  and  $t_{*,100}$  for each individual core, the latter of which is undefined for some sink particles that merge with another particle. The horizontal dashed line in panel (b) marks the asymptotic accretion rate of the LP flow defined in Equation (40). Right panels show accretion statistics for all cores in model M10. (c) The distribution of the inflow rate measured at  $r = R_{\text{core}}$  and  $t = t_{\text{crit}}$ . (d) The distribution of the time-averaged accretion rates at  $r = R_{\text{core}}$  (orange histogram) and  $r = 0$  (green histogram). The average is taken during the interval  $[t_{\text{coll}}, t_{*,100}]$ , except some cases where core tracking stopped before  $t_{*,100}$ .

tion efficiency of 100%)<sup>4</sup>. The period of time between  $t_{\text{coll}}$  and  $t_{*,100}$  corresponds to the “envelope infall” stage

of Gong & Ostriker (2009), for which we define

$$\Delta t_{\text{infall}} \equiv t_{*,100} - t_{\text{coll}}. \quad (41)$$

<sup>4</sup> In reality, the accretion after  $t_{\text{coll}}$  would be affected by winds and radiation from a protostellar system, which are not included in our simulations.

Figure 9(c) shows that  $\Delta t_{\text{infall}}$  is typically shorter than the free-fall time associated with the mean core den-

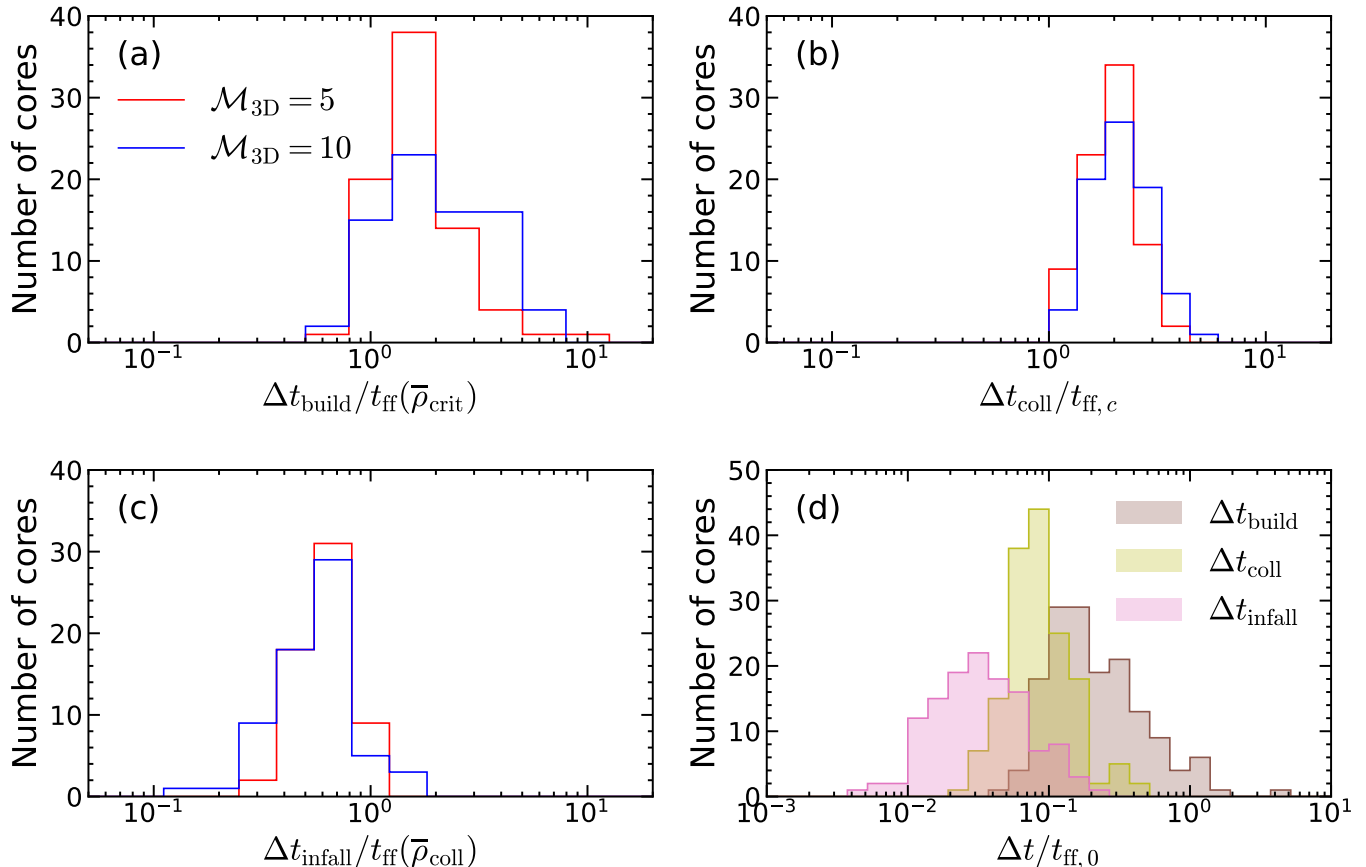


**Figure 9.** The distributions of the measured durations that a core spends in (a) the core building stage ( $\Delta t_{\text{build}}$ ), (b) the core collapse stage ( $\Delta t_{\text{coll}}$ ), and (c) the envelope infall stage ( $\Delta t_{\text{infall}}$ ), for cores in model M5 (red) and M10 (blue). The timescales are normalized by gravitational free-fall times at a density appropriate for each stage. (d) The comparison of the combined distributions of  $\Delta t_{\text{build}}$  (brown),  $\Delta t_{\text{coll}}$  (yellow), and  $\Delta t_{\text{infall}}$  (pink) for all cores in models M5 and M10; here the timescales are given in units of  $t_{\text{ff},0}$ , which is  $\sim 3\text{--}6$  Myr under typical GMC conditions (Equation (19)).

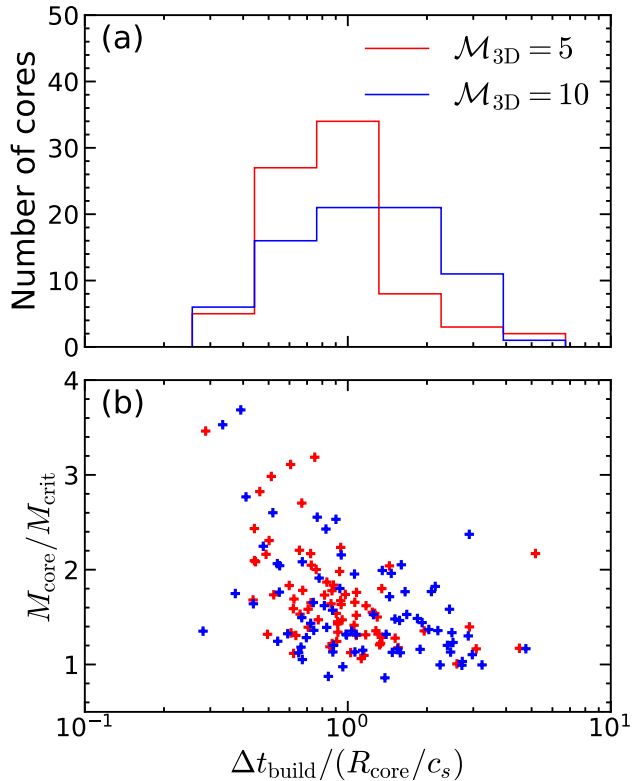
sity  $\bar{\rho}_{\text{coll}}$  at the end of the collapse<sup>5</sup>, with the median at  $\Delta t_{\text{infall}} = 0.6t_{\text{ff}}(\bar{\rho}_{\text{coll}})$ . This is not surprising considering that by the time  $t_{\text{coll}}$ , the core inflow has already achieved supersonic velocities (see Figure 12 in Paper II) such that it takes less time to reach the center compared to the free-fall from initially at rest. We note that Gong & Ostriker (2009, Figure 12) found  $\Delta t_{\text{infall}}/t_{\text{ff}}(\bar{\rho}_{\text{coll}}) \sim 0.8\text{--}1$  in their one-dimensional converging flow simulations.

Figure 8(b) shows that the sink mass continues to grow even after  $t_{*,100}$  without noticeable decline in the accretion rate. As previously pointed out by Gong & Ostriker (2015, see their Figure 20), this late accretion (in the terminology of Gong & Ostriker 2009) is expected

<sup>5</sup> As the collapse proceeds the mean density within the “Lagrangian radius”  $r_M$  enclosing  $M_{\text{core}}$  increases such that  $\bar{\rho}_{\text{coll}} \equiv M_{\text{core}}/(4\pi r_M^3/3) \sim 3\bar{\rho}_{\text{crit}}$ , where  $\bar{\rho}_{\text{crit}} \equiv M_{\text{core}}/(4\pi R_{\text{core}}^3/3)$ . The free-fall time correspondingly decreases to  $t_{\text{ff}}(\bar{\rho}_{\text{coll}}) \sim 0.6t_{\text{ff}}(\bar{\rho}_{\text{crit}})$ .

since cores are not isolated objects truncated at a finite radius, but instead are the inner parts of converging flows that continue to be accreted onto the sink particle. For example, Figure 8(d) indicates that the time-averaged inflow rate at  $r = R_{\text{core}}$  during the envelope infall stage is about a half as large as the sink particle accretion rate during the same time period.

In reality, however, the accreting flows likely arrive at a protostellar disk rather than directly onto the forming protostar, such that only a fraction of  $\dot{M}_{\text{in}}(r \rightarrow 0)$  would ultimately reach the protostellar surface. In addition, radiation and/or bipolar outflows from the forming protostar would limit the accretion rate during the envelope infall and late accretion stages for some systems (e.g., Hansen et al. 2012; Kuiper et al. 2016). However, the persistence of accretion after the initial core is consumed may be essential for the formation of massive stars. Based on our simulations, it does not appear possible for massive stars to originate as massive, highly turbulent, quasi-equilibrium cores that become super-



**Figure 10.** (a) The distribution of the ratio between the core building time (Equation (38)) and the sound crossing time for model M5 (red) and M10 (blue). (b) The ratio between the core mass to the critical mass versus the normalized core building time. The critical mass is calculated using Equation (10) with the measured average density  $\bar{\rho}$  and velocity dispersion  $\sigma_{1\text{D}}$  of each critical core. The median ratio is  $M_{\text{core}}/M_{\text{crit}} = 1.7$  and  $1.3$  for the range  $\Delta t_{\text{build}}/(R_{\text{core}}/c_s) < 1$  and  $> 1$ , respectively.

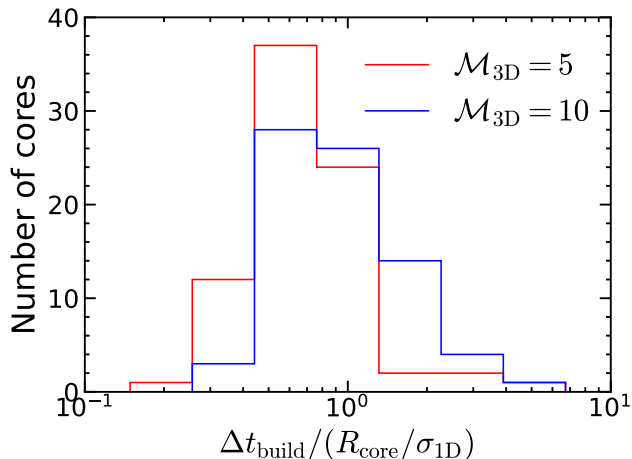


**Figure 11.** Similar to Figure 10(a), but for the building time normalized to the turbulent crossing time  $R_{\text{core}}/\sigma_{1\text{D}}$ .

critical and collapse. An alternative would be sustained accretion from a larger-scale converging flow.

Finally, Figure 9(d) compares  $\Delta t_{\text{build}}$ ,  $\Delta t_{\text{coll}}$ , and  $\Delta t_{\text{infall}}$  on a common scale, showing that the characteristic timescales becoming shorter and shorter as a core evolves to later stages. The median value for each stages are  $\Delta t_{\text{build}} \sim 0.19t_{\text{ff},0}$ ,  $\Delta t_{\text{coll}} \sim 0.085t_{\text{ff},0}$ , and  $\Delta t_{\text{infall}} \sim 0.032t_{\text{ff},0}$ , where  $t_{\text{ff},0} \sim 3\text{--}6$  Myr under typical GMC conditions (Equation (19)).

## 5. DISCUSSION

### 5.1. Is There a Threshold Density?

A recurring theme in star formation theory is that there exists a “threshold density” above which gas is gravitationally unstable. For example, based on different physical arguments and assumptions, Krumholz & McKee (2005) and Padoan & Nordlund (2011) proposed that there exists a threshold density above which a core becomes unstable and collapses. For a cloud with the virial parameter  $\alpha_{\text{vir}}$  and Mach number  $\mathcal{M}_{3\text{D}}$ , the threshold density (relative to the mean cloud value  $\rho_0$ ) predicted from these theories is  $\rho_{\text{thr}}/\rho_0 = (0.28\text{--}0.55) \times \alpha_{\text{vir}}\mathcal{M}_{3\text{D}}^2$  (the lower and upper ends correspond to the theory of Krumholz & McKee 2005 and Padoan & Nordlund 2011, respectively, with their fiducial choice of order-unity parameters; we assume  $p = 0.5$  for the former theory).

When applied to our models which have  $\alpha_{\text{vir}} = 2.06$ , the theories of Krumholz & McKee (2005) and Padoan & Nordlund (2011) predicts that the threshold density lies somewhere in between  $\rho_{\text{thr}}/\rho_0 = 14\text{--}28$  and  $58\text{--}113$  for models M5 and M10, respectively. Although the measured distributions of critical core density (Figure 5(c)) start to rise roughly around the predicted range of  $\rho_{\text{thr}}$ , the distribution extends widely above and below  $\rho_{\text{thr}}$ . This indicates that the threshold density of Krumholz & McKee (2005) or Padoan & Nordlund (2011) is neither a necessary nor sufficient condition for collapse of individual cores. Indeed, Figure 3 indicates that individual cores start to collapse at a wide range of densities, due both to the spatially varying strength of turbulence (Figure 2(a)), and to the varying tidal environment in which they are born.

Rather than a single threshold density, there may be a characteristic density set by the global parameters of a cloud, with more specific critical criteria responsive to local variations in conditions. We note that very different physical arguments lead to similar characteristic densities of gravitationally unstable cores. For example, considerations of anisotropic core formation mediated by magnetic fields in local converging flows lead to  $\rho_{\text{char}}/\rho_0 = 0.56\mathcal{M}_{3\text{D}}^2$  for  $\mathcal{M}_{3\text{D}}$  the flow Mach number



(Chen & Ostriker 2015, from Eqn. (6) and (7); see also Chen & Ostriker 2014). For  $\alpha_{\text{vir}} \sim 2$ , all these characteristic densities are comparable to a simple “post-shock” density  $\mathcal{M}_{3\text{D}}^2 \rho_0$  multiplied by some order unity coefficient.

The TES model provides a more mathematical route to a characteristic unstable-core density based on cloud-scale parameters, yielding a similar value to characteristic densities obtained from various physical arguments described above. Combining Equation (14) with Equation (12) (assuming  $p = 0.5$  and  $a = 0.9$ ) and Equation (21), the average density of critical cores forming under “typical” turbulence conditions (i.e.,  $r_s \sim r_{s,\text{cloud}}$ ) is

$$\begin{aligned} \frac{\rho_{\text{char}}}{\rho_0} &= 0.164 \left( \frac{\sigma_{1\text{D}}}{c_s} \right)^{-4} \left[ 1 + 0.5 \left( \frac{\sigma_{1\text{D}}}{c_s} \right)^2 \right]^{2/3} \alpha_{\text{vir}} \mathcal{M}_{3\text{D}}^2 \\ &\approx 0.48 \alpha_{\text{vir}} \mathcal{M}_{3\text{D}}^2, \end{aligned} \quad (42)$$

where we take  $\sigma_{1\text{D}} = 0.8c_s$  as a representative value (e.g., Figure 4(d)) in the second equality. For a cloud with  $\alpha_{\text{vir}} \sim 2$ , Equation (42) says that  $\rho_{\text{char}}$  is essentially the post-shock density,  $\mathcal{M}_{3\text{D}}^2 \rho_0$ , for an isothermal shock.

Of course, in order for collapse to occur, the core radius – which depends on the local tidal gravitational field – must exceed the critical radius. If we use the above  $\rho_{\text{char}}$  in Equation (9) and Equation (10), adopting  $\sigma_{1\text{D}}/c_s = 0.8$  as before, we find a characteristic radius and mass for critical cores of  $R_{\text{char}} = 0.67 L_{\text{J},0} / (\alpha_{\text{vir}}^{1/2} \mathcal{M}_{3\text{D}})$  and  $M_{\text{char}} = 0.63 M_{\text{J},0} / (\alpha_{\text{vir}}^{1/2} \mathcal{M}_{3\text{D}})$ , where Equation (16) and Equation (17) can be used to convert to physical units. For typical GMC parameters,  $R_{\text{char}} \sim 0.06 \text{ pc}$  and  $M_{\text{char}} \sim 1.5 M_{\odot}$ .

When considering the effects of turbulence, almost all theories assume that a single linewidth–size relation applies to all cores and that the turbulent velocities are completely independent of the density. However, Figure 2(a) (see also Figure 16 of Paper II) shows that both the slope and normalization of the *local* linewidth–size relations significantly vary from region to region. While we took  $r_s = r_{s,\text{cloud}}$  and  $p = 0.5$  in deriving Equation (42), in reality, these local variations in the turbulent scaling relations would modify the leading numerical coefficient in Equation (42) proportional to  $(r_s/r_{s,\text{cloud}})^{-2} \propto \sigma_{1\text{D}}^4$ , in addition to the variation in  $\sigma_{1\text{D}}/c_s$  of the square bracketed factors. This would lead to a range of critical densities at which collapse is triggered, as is seen in our distributions in Figure 5 (see also Figure 3). A more refined theory should therefore draw the turbulent velocity dispersion (or the local sonic

scale) from a joint distribution of density and velocity dispersion rather than assuming a single linewidth–size relation independent of density.

## 5.2. Absence of highly-turbulent cores

Our simulations show that the vast majority (96%) of the critical cores that are the immediate precursors of star formation have radial turbulent velocity dispersion  $\sigma_{1\text{D}} < 1.5c_s$ , and even the most turbulent critical core has  $\sigma_{1\text{D}} = 2.28c_s$ . That is, the turbulence is at most trans-sonic. Thus, we do not find evidence supporting the McKee & Tan (2003) theory (see also Myers & Fuller 1992; McLaughlin & Pudritz 1997), in which the precursors of massive stars are massive cores supported by turbulence.

From a physical point of view, the idea of massive cores supported primarily by turbulence suffers from two main difficulties. One is that highly supersonic turbulence would produce a high degree of substructure, so that even if a core has strong enough gravity to collapse, it would rapidly fragment rather than producing a single massive star. The second is that strong turbulence implies a flow crossing time comparable to the gravitational timescale, so that highly turbulent structures are also highly transient. For critical TESs, the ratio of the turbulent crossing time  $t_{\text{cross}} = R_{\text{core}}/\sigma_{1\text{D}}$  to the free-fall time at average density decreases from  $t_{\text{cross}}/t_{\text{ff}} = 1.6$  at  $\sigma_{1\text{D}}/c_s = 1$  to  $t_{\text{cross}}/t_{\text{ff}} = 0.82$  at  $\sigma_{1\text{D}}/c_s = 3$  (see also Figure 8(d) of Paper I). Figure 11 indicates that the median core building time  $t_{\text{build}}$  is a factor of 1.3 lower than the turbulent crossing time, and that less than 10% of cores have  $t_{\text{build}}/t_{\text{cross}} > 2$ . This suggests that massive, turbulently supported cores would self-destruct before they succeed in assembling enough mass to become unstable.

Recent high-resolution observations also do not find strong evidence of high-mass, highly turbulent prestellar cores (e.g., Sanhueza et al. 2019; Redaelli et al. 2022; Li et al. 2023; Morii et al. 2023; Nony et al. 2023); often, previous high-mass prestellar core candidates turn out to be protostellar in nature or resolved into a collection of lower-mass substructures when resolution is increased. Observed protostellar cores in high-mass star-forming regions are on average more massive than prestellar cores and have shallower CMF slope (Li et al. 2023; Nony et al. 2023), suggesting cores continue to grow in mass after collapse. Taken together, the lack of massive prestellar cores and the presence of continued accretion well beyond the time of collapse (e.g., Figure 8) support the idea that massive stars form by accretion flows from scales beyond the critical core (see Section 2.6.2 of Motte et al. 2018 for a review; see also

Padoan et al. 2020), rather than by collapse of massive, highly turbulent prestellar core.

### 5.3. *The CMF in Numerical Simulations*

Various theoretical arguments suggest that as a result of supersonic turbulence, the CMF defined by the number of cores per logarithmic mass bin has peak at a characteristic mass scale set by the large-scale physical conditions in the cloud (e.g., Equations (34) and (35), Gong & Ostriker 2011; Chen & Ostriker 2014, 2015; Haugbølle et al. 2018; see also Padoan & Nordlund 2002; Hennebelle & Chabrier 2008; Hopkins 2012 for related theories that make predictions for the whole CMF). Even if the full CMF does not directly map to the stellar initial mass function (IMF) due to late-stage accretion and disk fragmentation, a peak in the CMF could potentially have implications for the turnover of the IMF or the mass function of stellar systems, allowing for fragmentation into a binary or multiple at a later evolutionary stage (see e.g. review by Offner et al. 2023).

It has been questioned in the literature, however, whether cloud-scale conditions (including an effectively isothermal equation of state, given the balance of heating and cooling) and the physics of self-gravitating turbulence are ever able to imprint a characteristic mass scale, and if so, whether this is relevant to the IMF (e.g., Martel et al. 2006; Federrath et al. 2017; Guszejnov et al. 2018, 2020, see also Section 5 of Hennebelle & Grudić 2024 for a recent review). Regarding the first question, it has been suggested that non-convergence of mass functions is a general feature of self-gravitating, isothermal numerical simulations. For example, Guszejnov et al. (2018) found no convergence with increasing numerical resolution in the low-mass spectrum of the SMF for their isothermal, unmagnetized self-gravitating turbulence simulations, and Guszejnov et al. (2020, see their Figure 10) found lack of convergence in the low mass end of the SMF in their isothermal magnetohydrodynamic (MHD) simulations. Although their specific results regarding lack of low-mass convergence may have been compromised by an error in their sink particle implementation (see Guszejnov et al. 2021), a more general issue is that this approach does not distinguish between convergence in the CMF and convergence in the SMF.

Indeed, when discussing numerical convergence of mass functions, most studies have presented results based on the SMF rather than the CMF (e.g., Martel et al. 2006; Federrath et al. 2017; Guszejnov et al. 2018; Lee & Hennebelle 2018; Haugbølle et al. 2018; see, however, Chen & Ostriker 2014, 2015; Gong & Ostriker 2015; Padoan et al. 2020; Pelkonen et al. 2021 for the CMF). While the CMF in observations reflects cloud-scale dy-

namics and choices in segmentation algorithms, and the CCMF studied in the present work focuses on the initial conditions for formation of star-disk systems, additional effects (both physical and numerical) enter in determining the SMF in simulations, so that one does not necessarily map to the other. Collapsing cores or disks may fragment (although the fragmentation *during* core collapse may be difficult; see Tohline 1980a,b; Hanawa & Matsumoto 1999; Lai 2000; Sugimura et al. 2017), and cores that collapse may continue to accrete, growing in mass (as shown by Figure 8; see also Padoan et al. 2020; Pelkonen et al. 2021). The SMF measured at any given moment will include young sink particles that have accreted only a small fraction of the parental core mass, as well as old sink particles that become overmassive through sustained accretion if realistic feedback is not included. Additionally, the SMF may include spurious sink particles formed in unresolved cores that would otherwise have been torn apart by turbulence at higher resolution, and low-mass sinks forming within disks around sink particles at late stages of evolution. Disk fragmentation is subject to tidal forces and heating once a central protostar has formed (see Kratter & Lodato 2016, for a review), and while these effects are important in setting the IMF they are not relevant to the cloud-scale gravo-turbulent fragmentation process. The SMF can also be affected by the choice of subgrid model parameters, as shown by Haugbølle et al. (2018, Appendix C). Thus, in order to properly distinguish the roles of gravo-turbulent fragmentation on cloud scales from disk-scale fragmentation, we strongly encourage measuring and studying CMFs in numerical simulations. Although there is no single “correct” definition of a prestellar core, the criteria we have developed based on the theoretical critical radius compared to the tidal radius (and transition from positive to negative net force) provide physically motivated definitions, which leads to the CCMF in this work. Following the full history prior to, during, and subsequent to collapse would be necessary to test theories of the CMF and to understand the relation between the CMF and the IMF.

To claim the existence or absence of numerically converged mass function (whether it is the CMF or the SMF), it is necessary to achieve numerical resolution high enough to unambiguously resolve the anticipated characteristic mass. In Appendix A, we intercompare various measures of numerical resolution in recent self-gravitating turbulence simulations, which is relevant to the question of numerical convergence in mass functions.

## 6. SUMMARY AND CONCLUSIONS

Prestellar cores form within turbulent GMCs and undergo gravitational runaway at some point in their life, leading to star formation. To understand the physical processes responsible for triggering collapse, it is essential to investigate the detailed evolution of individual cores and their physical properties at the onset of collapse. In the companion paper (Paper II), we have conducted a comprehensive analysis of the evolution of individual cores, using a carefully constructed suite of numerical simulations of turbulent, self-gravitating clouds. In this work, we investigate the structure and physical properties of these cores measured at the *critical time* when they initiate collapse (Section 3), and interpret these results using our new model for TESs developed in Paper I. We also measure the inflow rates before and after the collapse, which determine the timescales the cores spend in each evolutionary stage (Section 4).

Our main conclusions are as follows:

1. Within cores, the turbulent velocity dispersion increases with distance  $r$  approximately as a power-law (Figure 2(a)), validating the main assumption of the TES model developed in Paper I. The measured radial density profiles are consistent with the theoretical prediction of the TES model for both quiescent and highly turbulent cores (Figure 1). The BE sphere profile is too steep to explain the density structure of turbulent cores.
2. The cores in our simulations have subsonic or transonic internal velocity dispersions ( $\sigma_{1D} \sim 0.5\text{--}1.5c_s$ ) at the onset of the collapse (Figure 4(d)), consistent with observed superthermal linewidths (e.g., Lee et al. 1999, 2001; Foster et al. 2009; Friesen et al. 2009, 2010; Lee et al. 2014; Storm et al. 2016; Kirk et al. 2017; Tang et al. 2018; Chen et al. 2019; Kerr et al. 2019; Choudhury et al. 2021; Li et al. 2023). The slope of the internal linewidth–size relation of cores is  $p \sim 0.5 \pm 0.2$  (Figure 4(a)), similar to the slope of the linewidth–size relation on large scales in our simulations (and observed GMCs). We do not find evidence for highly turbulent, massive prestellar cores (see Section 5.2 for related discussion). However, we do find evidence for continued accretion beyond the core collapse (Figure 8(b)), which may be responsible for the formation of massive stars.
3. The building, collapse, and infall stages of core evolution have successively shorter durations (Figure 9), decreasing from a median of 0.19 to 0.085 to 0.032 times the free-fall time  $t_{ff,0}$  at the mean density of the surrounding cloud. This implies that observed timescales would become shorter as

cores evolve from prestellar to protostellar phases. Since the mean core densities are  $\sim 100$  times average cloud values, the duration of prestellar evolutionary stages is  $\sim 3$  times the internal free-fall time within the critical cores. Core building takes only a single sound crossing time (Figure 10), indicating that cores form rapidly by dynamical compression rather than quasi-static processes. The prolonged collapse duration relative to the central free-fall time,  $\Delta t_{\text{coll}} \sim 2t_{ff,c}$ , is consistent with the small net force applied throughout the collapse (Paper II).

4. Cores form at a wide range of densities (Figure 5), with most having a center-to-edge density contrast of  $\sim 10\text{--}30$  (here, “edge” means  $r = r_{\text{crit}}$ ), consistent with theoretical expectations based on the TES model in Paper I with at most transonic internal turbulence. The distribution of ratios of the core internal density to the mean cloud density on large scales peaks at  $\bar{\rho}/\rho_0 \sim 100$  for both our M5 and M10 models (although the peak would likely shift to higher densities for model M10 when resolution is increased), extending down to  $\sim 10$  for M10, and lower for M5. There is no sign of a single threshold density for collapse, as has been proposed in some theories for determining the star formation rate in molecular clouds. Local variations in the turbulence strength are significant even within a single cloud, affecting the density at which cores become unstable (Figures 2 and 3). The distribution of critical core densities is directly related to the CMF, which shows marginal evidence of a peak consistent with a characteristic post-shock critical mass  $M_{\text{char, trb}}$  associated with the initial cloud-scale Mach number (Figure 6(a)). Resolving the peak of the CMF requires the minimum resolvable mass far smaller than the characteristic mass, which becomes increasingly challenging for higher Mach number (Appendix A).
5. Prestellar cores – i.e. the immediate precursors of stars, as measured at  $t_{\text{crit}}$  – have distinctive structural and dynamic properties, marking this as a key stage of star formation. However, our analysis implies that the CMF does not map directly to the IMF, at least on the high-mass end. In particular, we do not find evidence for massive prestellar cores supported by turbulence. Instead, given that the mass accretion rate measured at a fixed radius,  $\dot{M}_{\text{in}}(r = R_{\text{core}})$  stays roughly constant or even slightly increases both before and after the collapse (Figure 8(a)), our results sug-

gest that more massive stars may form due to sustained accretion. After the sink particle forms, its accretion rate (which in a real system would be the onto a circumstellar disk) remains at a steady level  $\sim (10\text{--}20)c_s^3/G$  (Figure 8(b),(d)), comparable to  $\dot{M}_{\text{in}}(r = R_{\text{core}})$ .

As noted in Paper II, a limitation of the present set of simulations is the absence of magnetic fields. It will be very interesting to consider models with varying magnetic field strength, in order to test whether the properties of critical cores end up being consistent with anisotropic model outlined in Chen & Ostriker (2014, 2015), in the sense of evolving to become magnetically supercritical by inflow along magnetic fields (reaching  $v_A \sim c_s$ ), while simultaneously also having similar turbulence properties (with  $\sigma_{1D} \sim c_s$ ) to cores in the present simulations. It will be also interesting to examine how projection effects map the intrinsic power-law structure function found within the critical cores to ob-

served linewidth–size relation, as discussed in Paper I. Our preliminary analysis indicates that, even though the intrinsic turbulent velocity dispersion grows in radius as a power law within cores, the line-of-sight velocity dispersion flattens toward the center in the sky plane due to the density-weighted projection effect. This implies that observed “coherent cores,” which have roughly constant non-thermal velocity dispersion profiles and shallower-than-BE density profiles (e.g., Goodman et al. 1998; Pineda et al. 2010; Chen et al. 2019) might be supported by turbulence, and evolving toward the onset of collapse.

- 1 This work was supported in part by grant 510940 from
- 2 the Simons Foundation to E. C. Ostriker. Computa-
- 3 tional resources for this project were provided by Prince-
- 4 ton Research Computing, a consortium including PIC-
- 5 SciE and OIT at Princeton University.

## REFERENCES

- André, P., Di Francesco, J., Ward-Thompson, D., et al. 2014, in *Protostars and Planets VI*, ed. H. Beuther, R. S. Klessen, C. P. Dullemond, & T. Henning, 27–51, doi: [10.2458/azu\\_uapress.9780816531240-ch002](https://doi.org/10.2458/azu_uapress.9780816531240-ch002)
- Andre, P., Ward-Thompson, D., & Barsony, M. 2000, in *Protostars and Planets IV*, ed. V. Mannings, A. P. Boss, & S. S. Russell, 59, doi: [10.48550/arXiv.astro-ph/9903284](https://doi.org/10.48550/arXiv.astro-ph/9903284)
- Bergin, E. A., & Tafalla, M. 2007, *ARA&A*, 45, 339, doi: [10.1146/annurev.astro.45.071206.100404](https://doi.org/10.1146/annurev.astro.45.071206.100404)
- Bonnor, W. B. 1956, *MNRAS*, 116, 351, doi: [10.1093/mnras/116.3.351](https://doi.org/10.1093/mnras/116.3.351)
- Chen, C.-Y., & Ostriker, E. C. 2014, *ApJ*, 785, 69, doi: [10.1088/0004-637X/785/1/69](https://doi.org/10.1088/0004-637X/785/1/69)
- . 2015, *ApJ*, 810, 126, doi: [10.1088/0004-637X/810/2/126](https://doi.org/10.1088/0004-637X/810/2/126)
- Chen, C.-Y., Storm, S., Li, Z.-Y., et al. 2019, *MNRAS*, 490, 527, doi: [10.1093/mnras/stz2633](https://doi.org/10.1093/mnras/stz2633)
- Choudhury, S., Pineda, J. E., Caselli, P., et al. 2021, *A&A*, 648, A114, doi: [10.1051/0004-6361/202039897](https://doi.org/10.1051/0004-6361/202039897)
- Collins, D. C., Le, D. K., & Jimenez Vela, L. L. 2024, *MNRAS*, 532, 681, doi: [10.1093/mnras/stae1493](https://doi.org/10.1093/mnras/stae1493)
- di Francesco, J., Evans, N. J., I., Caselli, P., et al. 2007, in *Protostars and Planets V*, ed. B. Reipurth, D. Jewitt, & K. Keil, 17, doi: [10.48550/arXiv.astro-ph/0602379](https://doi.org/10.48550/arXiv.astro-ph/0602379)
- Ebert, R. 1955, *ZA*, 37, 217
- . 1957, *ZA*, 42, 263
- Federrath, C., Krumholz, M., & Hopkins, P. F. 2017, in *Journal of Physics Conference Series*, Vol. 837, *Journal of Physics Conference Series (IOP)*, 012007, doi: [10.1088/1742-6596/837/1/012007](https://doi.org/10.1088/1742-6596/837/1/012007)
- Foster, J. B., Rosolowsky, E. W., Kauffmann, J., et al. 2009, *ApJ*, 696, 298, doi: [10.1088/0004-637X/696/1/298](https://doi.org/10.1088/0004-637X/696/1/298)
- Foster, P. N., & Chevalier, R. A. 1993, *ApJ*, 416, 303, doi: [10.1086/173236](https://doi.org/10.1086/173236)
- Friesen, R. K., Di Francesco, J., Shimajiri, Y., & Takakuwa, S. 2010, *ApJ*, 708, 1002, doi: [10.1088/0004-637X/708/2/1002](https://doi.org/10.1088/0004-637X/708/2/1002)
- Friesen, R. K., Di Francesco, J., Shirley, Y. L., & Myers, P. C. 2009, *ApJ*, 697, 1457, doi: [10.1088/0004-637X/697/2/1457](https://doi.org/10.1088/0004-637X/697/2/1457)
- Gong, H., & Ostriker, E. C. 2009, *ApJ*, 699, 230, doi: [10.1088/0004-637X/699/1/230](https://doi.org/10.1088/0004-637X/699/1/230)
- . 2011, *ApJ*, 729, 120, doi: [10.1088/0004-637X/729/2/120](https://doi.org/10.1088/0004-637X/729/2/120)
- Gong, M., & Ostriker, E. C. 2015, *ApJ*, 806, 31, doi: [10.1088/0004-637X/806/1/31](https://doi.org/10.1088/0004-637X/806/1/31)
- Goodman, A. A., Barranco, J. A., Wilner, D. J., & Heyer, M. H. 1998, *ApJ*, 504, 223, doi: [10.1086/306045](https://doi.org/10.1086/306045)
- Guszejnov, D., Grudić, M. Y., Hopkins, P. F., Offner, S. S. R., & Faucher-Giguère, C.-A. 2020, *MNRAS*, 496, 5072, doi: [10.1093/mnras/staa1883](https://doi.org/10.1093/mnras/staa1883)
- . 2021, *MNRAS*, 500, 1125, doi: [10.1093/mnras/staa3413](https://doi.org/10.1093/mnras/staa3413)
- Guszejnov, D., Hopkins, P. F., Grudić, M. Y., Krumholz, M. R., & Federrath, C. 2018, *MNRAS*, 480, 182, doi: [10.1093/mnras/sty1847](https://doi.org/10.1093/mnras/sty1847)

- Hanawa, T., & Matsumoto, T. 1999, *ApJ*, 521, 703, doi: [10.1086/307564](https://doi.org/10.1086/307564)
- Hansen, C. E., Klein, R. I., McKee, C. F., & Fisher, R. T. 2012, *ApJ*, 747, 22, doi: [10.1088/0004-637X/747/1/22](https://doi.org/10.1088/0004-637X/747/1/22)
- Haugbølle, T., Padoan, P., & Nordlund, Å. 2018, *ApJ*, 854, 35, doi: [10.3847/1538-4357/aaa432](https://doi.org/10.3847/1538-4357/aaa432)
- Hennebelle, P., & Chabrier, G. 2008, *ApJ*, 684, 395, doi: [10.1086/589916](https://doi.org/10.1086/589916)
- Hennebelle, P., & Grudić, M. Y. 2024, *ARA&A*, 62, 63, doi: [10.1146/annurev-astro-052622-031748](https://doi.org/10.1146/annurev-astro-052622-031748)
- Hopkins, P. F. 2012, *MNRAS*, 423, 2037, doi: [10.1111/j.1365-2966.2012.20731.x](https://doi.org/10.1111/j.1365-2966.2012.20731.x)
- Hunter, C. 1977, *ApJ*, 218, 834, doi: [10.1086/155739](https://doi.org/10.1086/155739)
- Kerr, R., Kirk, H., Di Francesco, J., et al. 2019, *ApJ*, 874, 147, doi: [10.3847/1538-4357/ab0c08](https://doi.org/10.3847/1538-4357/ab0c08)
- Kirk, H., Friesen, R. K., Pineda, J. E., et al. 2017, *ApJ*, 846, 144, doi: [10.3847/1538-4357/aa8631](https://doi.org/10.3847/1538-4357/aa8631)
- Könyves, V., André, P., Men'shchikov, A., et al. 2015, *A&A*, 584, A91, doi: [10.1051/0004-6361/201525861](https://doi.org/10.1051/0004-6361/201525861)
- Kratter, K., & Lodato, G. 2016, *ARA&A*, 54, 271, doi: [10.1146/annurev-astro-081915-023307](https://doi.org/10.1146/annurev-astro-081915-023307)
- Krumholz, M. R., & McKee, C. F. 2005, *ApJ*, 630, 250, doi: [10.1086/431734](https://doi.org/10.1086/431734)
- Kuiper, R., Turner, N. J., & Yorke, H. W. 2016, *ApJ*, 832, 40, doi: [10.3847/0004-637X/832/1/40](https://doi.org/10.3847/0004-637X/832/1/40)
- Lai, D. 2000, *ApJ*, 540, 946, doi: [10.1086/309361](https://doi.org/10.1086/309361)
- Larson, R. B. 1969, *MNRAS*, 145, 271, doi: [10.1093/mnras/145.3.271](https://doi.org/10.1093/mnras/145.3.271)
- Lee, C. W., Myers, P. C., & Tafalla, M. 1999, *ApJ*, 526, 788, doi: [10.1086/308027](https://doi.org/10.1086/308027)
- . 2001, *ApJS*, 136, 703, doi: [10.1086/322534](https://doi.org/10.1086/322534)
- Lee, K. I., Fernández-López, M., Storm, S., et al. 2014, *ApJ*, 797, 76, doi: [10.1088/0004-637X/797/2/76](https://doi.org/10.1088/0004-637X/797/2/76)
- Lee, Y.-N., & Hennebelle, P. 2018, *A&A*, 611, A89, doi: [10.1051/0004-6361/201731523](https://doi.org/10.1051/0004-6361/201731523)
- Li, S., Sanhueza, P., Zhang, Q., et al. 2023, *ApJ*, 949, 109, doi: [10.3847/1538-4357/acc58f](https://doi.org/10.3847/1538-4357/acc58f)
- Martel, H., Evans, Neal J., I., & Shapiro, P. R. 2006, *ApJS*, 163, 122, doi: [10.1086/500090](https://doi.org/10.1086/500090)
- McKee, C. F., & Ostriker, E. C. 2007, *ARA&A*, 45, 565, doi: [10.1146/annurev.astro.45.051806.110602](https://doi.org/10.1146/annurev.astro.45.051806.110602)
- McKee, C. F., & Tan, J. C. 2003, *ApJ*, 585, 850, doi: [10.1086/346149](https://doi.org/10.1086/346149)
- McLaughlin, D. E., & Pudritz, R. E. 1997, *ApJ*, 476, 750, doi: [10.1086/303657](https://doi.org/10.1086/303657)
- Moon, S., & Ostriker, E. C. 2024a, *ApJ*, 975, 295, doi: [10.3847/1538-4357/ad7813](https://doi.org/10.3847/1538-4357/ad7813)
- . 2024b, arXiv e-prints, arXiv:2411.07349, <https://arxiv.org/abs/2411.07349>
- Morii, K., Sanhueza, P., Nakamura, F., et al. 2023, *ApJ*, 950, 148, doi: [10.3847/1538-4357/accea](https://doi.org/10.3847/1538-4357/accea)
- Motte, F., Bontemps, S., & Louvet, F. 2018, *ARA&A*, 56, 41, doi: [10.1146/annurev-astro-091916-055235](https://doi.org/10.1146/annurev-astro-091916-055235)
- Myers, P. C., & Fuller, G. A. 1992, *ApJ*, 396, 631, doi: [10.1086/171744](https://doi.org/10.1086/171744)
- Nony, T., Galván-Madrid, R., Motte, F., et al. 2023, *A&A*, 674, A75, doi: [10.1051/0004-6361/202244762](https://doi.org/10.1051/0004-6361/202244762)
- Offner, S. S. R., Clark, P. C., Hennebelle, P., et al. 2014, in *Protostars and Planets VI*, ed. H. Beuther, R. S. Klessen, C. P. Dullemond, & T. Henning, 53–75, doi: [10.2458/azu\\_uapress\\_9780816531240-ch003](https://doi.org/10.2458/azu_uapress_9780816531240-ch003)
- Offner, S. S. R., Moe, M., Kratter, K. M., et al. 2023, in *Astronomical Society of the Pacific Conference Series*, Vol. 534, *Protostars and Planets VII*, ed. S. Inutsuka, Y. Aikawa, T. Muto, K. Tomida, & M. Tamura, 275, doi: [10.48550/arXiv.2203.10066](https://doi.org/10.48550/arXiv.2203.10066)
- Offner, S. S. R., Taylor, J., Markey, C., et al. 2022, *MNRAS*, 517, 885, doi: [10.1093/mnras/stac2734](https://doi.org/10.1093/mnras/stac2734)
- Padoan, P., Federrath, C., Chabrier, G., et al. 2014, in *Protostars and Planets VI*, ed. H. Beuther, R. S. Klessen, C. P. Dullemond, & T. Henning, 77–100, doi: [10.2458/azu\\_uapress\\_9780816531240-ch004](https://doi.org/10.2458/azu_uapress_9780816531240-ch004)
- Padoan, P., & Nordlund, Å. 2002, *ApJ*, 576, 870, doi: [10.1086/341790](https://doi.org/10.1086/341790)
- . 2011, *ApJ*, 730, 40, doi: [10.1088/0004-637X/730/1/40](https://doi.org/10.1088/0004-637X/730/1/40)
- Padoan, P., Pan, L., Juvela, M., Haugbølle, T., & Nordlund, Å. 2020, *ApJ*, 900, 82, doi: [10.3847/1538-4357/abaa47](https://doi.org/10.3847/1538-4357/abaa47)
- Pelkonen, V. M., Padoan, P., Haugbølle, T., & Nordlund, Å. 2021, *MNRAS*, 504, 1219, doi: [10.1093/mnras/stab844](https://doi.org/10.1093/mnras/stab844)
- Penston, M. V. 1969, *MNRAS*, 144, 425, doi: [10.1093/mnras/144.4.425](https://doi.org/10.1093/mnras/144.4.425)
- Pineda, J. L., Goldsmith, P. F., Chapman, N., et al. 2010, *ApJ*, 721, 686, doi: [10.1088/0004-637X/721/1/686](https://doi.org/10.1088/0004-637X/721/1/686)
- Redaelli, E., Bovino, S., Sanhueza, P., et al. 2022, *ApJ*, 936, 169, doi: [10.3847/1538-4357/ac85b4](https://doi.org/10.3847/1538-4357/ac85b4)
- Sanhueza, P., Contreras, Y., Wu, B., et al. 2019, *ApJ*, 886, 102, doi: [10.3847/1538-4357/ab45e9](https://doi.org/10.3847/1538-4357/ab45e9)
- Storm, S., Mundy, L. G., Lee, K. I., et al. 2016, *ApJ*, 830, 127, doi: [10.3847/0004-637X/830/2/127](https://doi.org/10.3847/0004-637X/830/2/127)
- Sugimura, K., Mizuno, Y., Matsumoto, T., & Omukai, K. 2017, *MNRAS*, 469, 4022, doi: [10.1093/mnras/stx1129](https://doi.org/10.1093/mnras/stx1129)
- Tang, M., Liu, T., Qin, S.-L., et al. 2018, *ApJ*, 856, 141, doi: [10.3847/1538-4357/aaadad](https://doi.org/10.3847/1538-4357/aaadad)
- Tohline, J. E. 1980a, *ApJ*, 235, 866, doi: [10.1086/157688](https://doi.org/10.1086/157688)
- . 1980b, *ApJ*, 239, 417, doi: [10.1086/158125](https://doi.org/10.1086/158125)

**Table 1.** Summary of the simulation parameters in selected works

Model	$\mathcal{M}_{3D}$	$\Delta x/L_{J,0}$	$\Delta m/M_{J,0}$	$M_{\text{char,th}}/M_{J,0}$	$M_{\text{min}}/M_{J,0}$	$M_{\text{min}}/M_{\text{char,th}}$	$\Delta x(\rho_0)/r_{s,\text{cloud}}$
(1)	(2)	(3)	(4)	(5)	(6)	(7)	(8)
M5 (this work)	5	$3.9 \times 10^{-3}$	-	$6.6 \times 10^{-2}$	$2.4 \times 10^{-2}$	0.36	0.043
M10 (this work)	10	$3.9 \times 10^{-3}$	-	$3.3 \times 10^{-2}$	$2.4 \times 10^{-2}$	0.72	0.087
M2e3_R3 (Guszejnov et al. 2020)	9.3	-	$5.4 \times 10^{-7}$	$3.6 \times 10^{-2}$	$1.2 \times 10^{-3}$	0.032	0.17
M2e4_R10 (Guszejnov et al. 2020)	16	-	$1.4 \times 10^{-6}$	$2.1 \times 10^{-2}$	$3.0 \times 10^{-3}$	0.14	0.39
M2e5_R30 (Guszejnov et al. 2020)	29	-	$8.5 \times 10^{-6}$	$1.1 \times 10^{-2}$	$1.8 \times 10^{-2}$	1.6	1.3
high (Haugbølle et al. 2018)	10	$3.4 \times 10^{-4}$	-	$3.3 \times 10^{-2}$	$2.1 \times 10^{-3}$	0.063	0.35
M8L2N512 (Gong & Ostriker 2015)	-	$2.0 \times 10^{-3}$	-	$8.6 \times 10^{-2}$	$1.2 \times 10^{-2}$	0.14	-

NOTE—Columns (3) and (4) provide the highest resolution (i.e., smallest  $\Delta x$  for Eulerian simulations and smallest  $\Delta m$  for Lagrangian simulations) of the models used for convergence study given in Column (1). All simulations are inherently scale-free and the choice of  $L_{J,0}$  and  $M_{J,0}$  is arbitrary. Because Guszejnov et al. (2020) and Haugbølle et al. (2018) present their results in physical units, we provide their adopted values for convenience:  $L_{J,0} = 1.3$  pc,  $M_{J,0} = 37 M_{\odot}$  (M2e3\_R3);  $L_{J,0} = 2.4$  pc,  $M_{J,0} = 71 M_{\odot}$  (M2e4\_R10);  $L_{J,0} = 4.0$  pc,  $M_{J,0} = 120 M_{\odot}$  (M2e5\_R30);  $L_{J,0} = 0.71$  pc,  $M_{J,0} = 17 M_{\odot}$  (high). Because the inflow Mach numbers in Gong & Ostriker (2015) cannot be directly related to  $\mathcal{M}_{3D}$ , we use the directly measured post-shock density to calculate  $M_{\text{char,th}}$  rather than from Equation (34) (see text). For the same reason, it is not straightforward to infer  $r_{s,\text{cloud}}$  in their simulations; we thus leave it out in this table.

## APPENDIX

### A. NUMERICAL RESOLUTION IN GRAVO-TURBULENT SIMULATIONS

To cross-compare the numerical resolutions of different simulations that have been used to address the question of numerical convergence of mass functions, Table 1 lists resolution parameters in some recent simulations, including this work. Column (1) gives the model name and reference. Column (2) gives the cloud-scale Mach number. Columns (3) and (4) give the numerical resolution  $\Delta x$  and  $\Delta m$  for fixed spatial- and fixed mass-resolution simulations, respectively, normalized by the Jeans scales at the mean cloud condition (for the adaptive mesh refinement (AMR) simulations, we indicate  $\Delta x$  at the highest refinement level). Column (5) gives the characteristic mass  $M_{\text{char,th}}$  from Equation (34). Column (6) gives the minimum resolvable mass  $M_{\text{min}}$  from Equations (23) and (24), adopting  $N_{\text{core,res}} = 8$  and using either  $\Delta x$  or  $\Delta m$  given in Columns (3)–(4). Column (7) gives the ratio  $M_{\text{min}}/M_{\text{char,th}}$ . Column (8) gives the numerical resolution at the mean density divided by the sonic scale, where we take the effective spatial resolution  $\Delta x(\rho_0) = (\Delta m/\rho_0)^{1/3}$  for fixed mass-resolution simulations.

If the core mass function peaks roughly around  $M_{\text{char,th}}$  predicted by various theories, clearly resolving the peak in numerical simulations would require  $M_{\text{min}}/M_{\text{char,th}} \ll 1$ . Combining Equations (23), (24) and (34), one can show that

$$\frac{M_{\text{min}}}{M_{\text{char,th}}} = 2.32 \mathcal{M}_{3D} N_{\text{core,res}} \left( \frac{\Delta x}{L_{J,0}} \right) \quad (\text{A1a})$$

$$= 12.5 \mathcal{M}_{3D} N_{\text{core,res}}^3 \left( \frac{\Delta m}{M_{J,0}} \right). \quad (\text{A1b})$$

This ratio is linearly proportional to the resolution (either  $\Delta x$  or  $\Delta m$  normalized to the Jeans scales at mean density), and is also linear in the Mach number, making it more difficult to resolve the peak of the CMF in higher Mach number simulations. Although Table 1 is far from being complete, Equation (A1) suggests that simulations should typically find the peak of the CMF (and possibly the SMF, modulo disk fragmentation) converges provided that  $M_{\text{min}}/M_{\text{char,th}}$  is sufficiently small. For our lower Mach number simulations, the ratio  $M_{\text{min}}/M_{\text{char,th}} = 0.36$ , while for our higher

Mach number simulations this ratio is 0.72. Thus, we expect to identify the CMF peak clearly in our M5 model but not in our M10, and indeed this appears consistent with our results.

The model [Guszejnov et al. \(2020\)](#) used for their SMF numerical convergence study (M2e5\_R30) has a fairly high Mach number  $\mathcal{M}_{3D} = 29$ , such that  $M_{\min}/M_{\text{char,th}} = 1.6$  at their highest mass resolution (i.e., smallest  $\Delta m = 10^{-3} M_{\odot} = 8.5 \times 10^{-6} M_{J,0}$ ). Thus, this set of numerical parameters would not be suitable for identifying the peak of CMF. However, the lower Mach number models in [Guszejnov et al. \(2020\)](#) (M2e3\_R3 and M2e4\_R10) have ratio  $M_{\min}/M_{\text{char,th}} = 0.032\text{--}0.14$ , making them suitable to resolve a CMF peak. Indeed, their rerun of model M2e4\_R10, after the error in the sink particle algorithm was corrected ([Guszejnov et al. 2021](#)), shows a peak in the SMF near  $M_{\text{char,th}} = 2.1 \times 10^{-2} M_{J,0} = 1.5 M_{\odot}$  (conversion to physical units adopting their sound speed and mean density).

In the AMR simulations of a  $\mathcal{M}_{3D} = 10$  cloud conducted by [Haugbølle et al. \(2018\)](#), the minimum resolvable mass at their highest refinement level ( $\Delta x = 50 \text{ au} = 3.4 \times 10^{-4} L_{J,0}$  adopting their mean cloud density and sound speed) is  $M_{\min} = 2.1 \times 10^{-3} M_{J,0} (N_{\text{core,res}}/8)$  from [Equation \(23\)](#). This leads to  $M_{\min}/M_{\text{char,th}} = 0.063$  if we adopt  $N_{\text{core,res}} = 8$ . [Pelkonen et al. \(2021\)](#) performed convergence analysis using the same simulation data of [Haugbølle et al. \(2018\)](#), finding that the SMF in their simulation converges to  $0.17 M_{\odot}$  with increasing numerical resolution. They also found that the corresponding progenitor core mass is  $0.26 M_{\odot} = 1.5 \times 10^{-2} M_{J,0}$ , which is a factor of 2.2 lower than  $M_{\text{char,th}}$ . We note that the CCMF in our model M5 also suggests a peak at a factor of  $\sim 2$  lower than  $M_{\text{char,th}}$  ([Figure 6\(a\)](#)), similar to the results of [Pelkonen et al. \(2021\)](#).

[Gong & Ostriker \(2015\)](#) performed local simulations focusing on a small portion of a GMC where the flows are supersonically converging, using an idealized converging flow setup. Due to the instability in the non-magnetized post-shock layer, their measured average density within the post-shock layer is only weakly dependent on the *inflow* Mach number such that [Equation \(34\)](#) is not straightforwardly applicable. Instead, we use their measured average post-shock density  $\rho_{\text{ps}} \sim 15\rho_0$  to estimate the characteristic mass  $M_{\text{char,th}} = M_{\text{BE}}(\bar{\rho} = \rho_{\text{ps}}) = 8.6 \times 10^{-2} M_{J,0}$ . The minimum resolvable mass at their highest resolution model with  $\Delta x = 2 \times 10^{-3} L_{J,0}$  is  $M_{\min} = 1.2 \times 10^{-2} M_{J,0} (N_{\text{core,res}}/8)$ , a factor of 7 lower than  $M_{\text{char,th}}$  for  $N_{\text{core,res}} = 8$ . They found that the peak of the CMF is numerically converged (see their [Figure 9](#)), with the measured peak location consistent with  $M_{\text{char,th}}$ . It is worth noting that [Gong & Ostriker \(2015\)](#) used the CMF constructed from the core masses measured at the end of collapse ( $t_{\text{coll}}$ ) for individual core.

Although we choose the resolution of our simulations carefully to resolve most of the core formation *by mass* (see [Section 3.3 of Paper II](#)), resolving the peak of the CMF poses a severe challenge because the mass fraction below the peak is very small. For example, if we assume the peak of the CMF occurs at  $M_{\text{peak}} \sim 0.5 M_{\text{char,th}}$  as it appears to be the case in this work and in [Pelkonen et al. \(2021\)](#), clear identification of the peak would require at least  $M_{\min} < (1/2) M_{\text{peak}} = 0.25 M_{\text{char,th}}$ . [Equation \(A1\)](#) then leads to the following resolution requirement for simulations with a fixed spatial resolution:

$$\frac{\Delta x}{L_{J,0}} < 1.35 \times 10^{-3} \left( \frac{N_{\text{core,res}}}{8} \right)^{-1} \left( \frac{\mathcal{M}_{3D}}{10} \right)^{-1}, \quad (\text{A2})$$

and the requirement for fixed mass resolution:

$$\frac{\Delta m}{M_{J,0}} < 3.91 \times 10^{-6} \left( \frac{N_{\text{core,res}}}{8} \right)^{-3} \left( \frac{\mathcal{M}_{3D}}{10} \right)^{-1}. \quad (\text{A3})$$

Considering that the size of the computational domain should be properly scaled with  $\mathcal{M}_{3D}$  to keep the cloud scale virial parameter constant, the total number of simulation elements for a uniform mesh would be

$$\begin{aligned} N^3 &= \left( \frac{L_{\text{box}}}{\Delta x} \right)^3 \\ &= (3012)^3 \left( \frac{N_{\text{core,res}}}{8} \right)^3 \left( \frac{\alpha_{\text{vir}}}{2} \right)^{-3/2} \left( \frac{\mathcal{M}_{3D}}{10} \right)^6, \end{aligned} \quad (\text{A4})$$

where we used [Equation \(20\)](#). Similarly, the required number of resolution elements for the fixed mass-resolution simulations is

$$\begin{aligned} N_p &\equiv \frac{M_{\text{box}}}{\Delta m} \\ &= 1.71 \times 10^7 \left( \frac{N_{\text{core,res}}}{8} \right)^3 \left( \frac{\alpha_{\text{vir}}}{2} \right)^{-3/2} \left( \frac{\mathcal{M}_{3D}}{10} \right)^4. \end{aligned} \quad (\text{A5})$$

We note that [Equations \(A4\) and \(A5\)](#) are minimum requirements and that even higher resolutions would be required to robustly demonstrate the numerical convergence of the identified peak.

Taken at face value, [Equations \(A4\) and \(A5\)](#) suggest that it might be easier to resolve the peak of the CMF by adopting a fixed mass-resolution rather than fixed spatial resolution. However, it is worth emphasizing that in addition to [Equation \(A2\)](#) for resolving cores, the effective spatial resolution in low-density regions must also be sufficiently high to resolve the sonic scale of turbulence. Column (8) of [Table 1](#) shows that, compared to other current simulations with adaptive resolution, the uniform resolution adopted in this work allows smaller  $\Delta x(\rho_0)/r_{s,\text{cloud}}$  and thus better resolves early nonlinear structures created by turbulence.

More generally, [Paper II](#) (see [Equation \(50\)](#) there) shows that resolving  $r_{s,\text{cloud}}$  imposes a resolution requirement that has the same Mach number scaling as [Equation \(A4\)](#). However, [Paper II](#) (see [Section 5.2](#) there) also demonstrated that the local sonic scale exhibits an order of magnitude variations (which is correlated with density) above and below  $r_{s,\text{cloud}}$ , which then demands higher resolution in moderate-density gas. To meet this additional requirement at mean cloud density, i.e.,  $\Delta x(\rho_0) \ll r_{s,\text{cloud}}$ , simulations adopting a fixed mass resolution need to satisfy not only [Equation \(A5\)](#) but also additionally

$$N_p = \frac{M_{\text{box}}}{\Delta m} = 1.90 \times 10^{10} \left( \frac{N_{s,\text{res}}}{30} \right)^3 \left( \frac{\mathcal{M}_{3\text{D}}}{10} \right)^6, \quad (\text{A6})$$

where  $N_{s,\text{res}} = r_{s,\text{cloud}}/\Delta x(\rho_0) = 30$  is recommended in [Paper II](#).<sup>6</sup> Thus, properly resolving the sonic scale is in fact more computationally challenging than resolving self-gravitating cores, whether for fixed mesh or moving mesh simulations.

<sup>6</sup> In [Paper II](#), we defined  $N_{s,\text{res}}$  with respect to sonic scale  $\lambda_{s,\text{cloud}} = (4/3)r_{s,\text{cloud}}$  and recommended  $\lambda_{s,\text{cloud}}/\Delta x = 40$ , which is equivalent to  $N_{s,\text{res}} = 30$  presented here.